The Mechanics of Initiation and Development of Thrust Faults and Thrust Ramps[1]

SARAH S. WIGGINTON[2,3]
ELIZABETH S. PETRIE[4]
JAMES P. EVANS[2]

---

[1] Manuscript received October 27, 2021; Accepted February 20, 2022.

[2] Department of Geosciences, Utah State University, 4505 Old Main Hill, Logan, UT 84322-4505, james.evans@usu.edu

[3] INTERA Inc, 3240 Richardson Road, Suite 2, Richland, Washington 99354, sarahwigginton92@gmail.com

[4] Department of Natural and Environmental Sciences, Western Colorado University, Gunnison, CO 81231, espetrie@western.edu

---

This peer-reviewed, and edited for publications manuscript has been published in The Mountain Geologist, v.59, #2, p. 47-76. This is the final version of this manuscript be found in 'Peer Reviewed' section of the Eartharxiv submission.

ABSTRACT

This study integrates the results of numerical modeling analyses based on outcrop studies and structural kinematic restorations to evaluate the mechanics of thrust fault initiation and development in mechanically layered sedimentary rocks. A field-based reconstruction of a mesoscopic thrust fault at Ketobe Knob in central Utah provides evidence of thrust ramp nucleation in competent units, and fault propagation upward and downward into weaker units at both fault tips. We investigate the effects of mechanical stratigraphy on stress heterogeneity, rupture direction, fold formation, and fault geometry motivated by the geometry of the Ketobe Knob thrust fault in central Utah; the finite element modeling examines how mechanical stratigraphy, load conditions, and fault configurations influence temporal and spatial variation in stress and strain. Our modeling focuses on the predicted deformation and stress distributions in four model domains: (1) an intact, mechanically stratified rock sequence, (2) a mechanically stratified section with a range of interlayer frictional strengths, and two faulted models, (3) one with a stress loading condition, and (4) one with a displacement loading condition. The models show that early stress increase in competent rock layers are accompanied by low stresses in the weaker rocks. The frictional models reveal that the heterogeneous stress variations increase contact frictional strength. Faulted models with a 20° dipping fault in the most competent unit result in stress increases above and below fault tips, with extremely high stresses predicted in a ‘back thrust’ location at the lower fault tip. These findings support the hypothesis that thrust faults and associated folds at the Ketobe Knob developed in accordance with a ramp-first kinematic model and development of structures was significantly influenced by the nature of the mechanical stratigraphy.

INTRODUCTION

The geometrical relationships and kinematic models used to explain the formation of structures in fold and thrust belts (Dahlstrom, 1970; Boyer and Elliott, 1982; Butler, 1982; Suppe, 1983; Cooper and Trayner, 1986; Suppe and Medwedeff, 1990) support a classic flat-ramp kinematic model of thrust fault propagation (Suppe and Medwedeff, 1990). The flat-ramp model is based on a thrust fault that nucleates on weak, shallowly dipping décollement horizons and propagates along décollement until the resistance to frictional slip on the flat is greater than resistance to brittle failure in rocks above the décollement. At this point faults propagate upward to form a ramp (Rich, 1934; Rodgers, 1950; Dahlstrom, 1970; Boyer and Elliott, 1982; Butler, 1982; Williams and Chapman, 1983; Mitra, 1990; McClay, 2011).

While this geometric/kinematic model is well documented in fold-and-thrust belts, it may not fully account for the mechanics and mechanisms by which thrust fault formation occurs. Integrating rock material properties and mechanical modeling with traditional field geology and kinematic analysis allows for investigations of different models for the development of thrust faults and folds (Chapple, 1970; Erickson, 1996; Underwood et al., 2003; Teixell and Koyi, 2003; Bourne, 2003; Welch et al., 2009; Roche et al., 2013; Hughes et al., 2014; Hughes and Shaw, 2015). Merging mechanics with kinematic models can help answer questions about the conditions that promote failure at thrust ramps, how stress state variations may promote failure, and the rock properties govern the continued propagation or arrest of newly formed thrust faults (Busetti and Fang, 2018).

The mechanical stratigraphy of rocks in thrust terrains may exert a control on nascent thrust fault formation (Eisenstadt and De Paor, 1987; Ferrill et al., 2017). Stress concentrations may form at imperfections in mechanically strong layers and stress heterogeneities at these sites in the stratigraphic system may cause faults to nucleate on the ramp and arrest in mechanically weak layers above and below (Eisenstadt and De Paor, 1987; Roche et al., 2013; Ferrill et al., 2016). Field evidence of this “ramp-first” faulting style is documented in mechanically layered formations at the sub-meter scale (Fig. 1; Eisenstadt and De Paor, 1987; McConnell et al., 1997; Ferrill et al., 2016) to the 10’s m scale (Ferrill et a., 2016;

Alsop et al., 2021) and map scales (Onderdonk et al., 2005; Newsom, 2015; Ferrill et al., 2016). Primary indicators of the ramp-first faulting style include the presence of fault propagation folds that form at both fault tips and a displacement or slip profile in which slip is largest in the center and decreases toward both fault tips (Ferrill et al., 2016; Alsop et al., 2021). These observations indicate that mechanical stratigraphy exerts an influence on the nucleation, propagation, and arrest of developing thrust faults, but more information is needed to describe the loading conditions that promote failure.

We integrate field-based structural analysis and two-dimensional cross section reconstructions (Wigginton, 2018), with the results of mechanical finite element models to investigate the effects of mechanical stratigraphy on stress heterogeneity, rupture direction, and thrust fault geometry. We use the results of field-based studies (Petrie et al., 2018; Wigginton, 2018) and their resulting kinematic models as the foundation for finite element mechanical models of small-displacement thrust fault development in rocks with contrasting mechanical strengths across layers and fault propagation folds in the hanging wall and footwall.

Background

Mechanical stratigraphy is the stratal expression of the contrasts in the cohesive, compressive, tensile, and frictional strengths of rock, along with the thicknesses of rock units and interface properties between mechanical units (Corbett et al., 1987; Gross et al., 1995; Underwood et al., 2003; Laubach et al., 2009; Ferrill et al., 2017; Hart and Cooper, 2021). Mechanical stratigraphy affects fault nucleation and propagation (Teixell and Koyi, 2003; Underwood et al., 2003; Laubach et al., 2009; Roche et al., 2013; Ferrill et al., 2017; Bracken, 2020), fracture nucleation location (Eisenstadt and De Paor, 1987; Ferrill et al., 2017), fault length, width, and the aperture across a slip surface (Laubach et al., 2009; McGinnis et al., 2017), fault-growth directions (King et al., 1988; Mitra and Mount, 1998), the proportions of folds and faults that form (Morley, 1994; Erickson, 1996), fold geometry (Fischer and Jackson, 1999; Gutiérrez-Alonso and Gross, 1999), fault-fold interactions (Chester, 2003), and fault shape and related fault zone deformation (Woodward and Rutherford, 1989; Pfiffner, 1993; Ferrill and Morris, 2008). Strong, competent units withstand higher stresses before deforming plastically (permanently) and they accommodate stress loads by brittle failure (Currie et al., 1962). Conversely, weak or incompetent strata deform plastically at lower stresses and may deform ductilely before fracturing in response to increased stress (Goodman, 1980). Stresses applied to mechanically layered sections with varying Young's moduli might lead to varying layer-parallel stresses within the anisotropic package (Roche et al., 2013). The highest stresses are expected to form in the competent units, and this is where faulting might initiate in some mechanically layered package (Eisenstadt and De Paor, 1987; Ferrill et al., 2016). This contrast in deformation styles between competent and incompetent rocks creates strong stress heterogeneity in mechanically layered systems.

The ramp-first fault model accounts for the impact of mechanically layered stratigraphy on thrust fault formation (Fig. 1). The influence of mechanically stratified formations requires models of thrust fault propagation wherein: 1) faults nucleate in structurally strong (stiff, low ductility) layers (i.e. brittle failure occurs), 2) they can propagate upward and downward, and 3) fault ramps form before the flats (Fig. 1; Chapman and Williams, 1985; Eisenstadt and De Paor, 1987; Ramsay, 1992; Tavani et al., 2006; Welch et al., 2009; Uzkeda et al., 2010; Ferrill et al., 2016; Alsop et al., 2021).

Primary lines of evidence of the ramp-first style include the development of up- and down-dip fault propagation folds (Williams and Chapman, 1983; Woodward, 1986, discussed in Fischer et al., 1992; Eisenstadt and De Paor, 1987; Ramsay, 1992; Schmidt et al., 1993; Morley, 1994; McConnell et al., 1997; Welch et al., 2009; Uzkeda et al., 2010; Ferrill et al., 2016; Alsop et al., 2021), and the slip distribution patterns along faults (McConnell et al., 1997; Ferrill et al., 2016; Marshak et al., 2019; Alsop et al., 2021). If a fault nucleates in a competent layer and propagates upward and downward, it is predicted to arrest in fault-tip folds in the more ductile layers above and below (Fig. 1). These asymmetric folds verge in the transport direction of the thrust fault. The dual-directional propagation of a thrust fault creates a hanging-wall anticline associated with the upward propagating tip and a footwall syncline associated with the downward propagating fault tip (Fig. 1). Fault slip patterns along a “ramp-first” fault slip decreases in both directions along faults (Ellis and Dunlap, 1988; McConnell et al., 1997; Apotria and Wilkerson, 2002;

Tavani et al., 2006; Cawood and Bond, 2020). All these features point to a potential influence of mechanical stratigraphy on the location, geometry, and direction of thrust fault development.

Previous models of the mechanics of thrust fault nucleation and fold formation used elastic dislocation models (Rodgers and Rizer, 1981), wax analogues (Odonne, 1990), two-dimensional (2D) numerical models (Reches and Eidelman, 1995), 2D numerical models of viscous flow around a fault (Grasemann et al., 2003), 2D finite element models of elasto-plastic deformation (Strayer and Hudleston, 1997), displacement field analysis (Grasemann et al., 2005), 2D kinematic plane strain models (Welch et al., 2009) and three-dimensional (3D) elastic numerical models (Roche et al., 2013). These studies produced a number of findings which bolster the ramp-first model of thrust fault propagation: 1) Odonne (1990) and Grasemann et al. (2005) found that displacement along the fault causes heterogeneous reorientation of the strain axes and the highest strains were found at the fault tips (Reches and Eidelman, 1995). Here the increased stresses were responsible for the development of fault- propagation folds, and the kinematic model of McConnell et al. (1997) for a dual edged fault propagation fold model is an excellent explanation of their results. 2) Models confined with overburden pressure produce significantly more stress heterogeneity around the fault and the degree of fault related folding likely depends partly on the depth of the fault (Odonne, 1990). 3) Low-angle faults (dips ~30°), are more likely to produce the fault-propagation-fold geometry (Grasemann et al., 2003; Grasemann et al., 2005). 4) The stress conditions that create fault-propagation folds are largely insensitive to the rheology of the rock (as long as the rheology is continuous and uniform), so fault propagation folds can form in any rock type (Reches and Eidelman 1995; Grasemann et al., 2005). 5) Relatively small differences in yield strengths can make a significant change to the sequence of failure in a sedimentary package (Roche et al., 2013). Roche et al. (2013) showed that for stratigraphic sequences with little variation in strength, nucleation occurs in the stiff layers (limestone or sandstone), while failure occurs in the compliant layer (claystone) if the stiff layer has high cohesion (Roche et al., 2013).

METHODS

In order to investigate the effects of mechanical stratigraphy on stress heterogeneity, rupture direction, and fault geometry we examined the Ketobe Knob thrust fault in Central Utah. The exposed thrust system exhibits characteristics of the ramp-first faulting style with a hanging wall anticline and large footwall syncline. In this section we briefly summarize the results of fieldwork and kinematic reconstructions which are the foundation for the numerical modeling (Wigginton, 2018). We describe in detail the methodology for generating the numerical finite element models of thrust fault formation.

A range of field analyses were conducted at the Ketobe Knob outcrop to characterize the structures and lithology including: 1) documentation the fold and fault geometries, 2) measurements of displacement along the length of the fault exposed at the Ketobe Knob outcrop, 3) documentation of mesoscopic structures, (e.g. slip surfaces on faults and bedding planes), 4) collection of rock samples for thin section analysis and XRD to characterize mineralogy and 5) collection of rebound values for each rock unit using a Schmidt hammer. The methodology and results of this field work are detailed in Wigginton (2018).

Restored cross sections were created in Move™, which contains a suite of algorithms to create/restore faults including Fault Parallel Flow, Elliptical Fault Flow, and three different kinematic fold/unfold algorithms that we utilized including Flexural Slip, Simple Shear, and Line Length (Petroleum Experts). A combination of these algorithms was applied to the structures on a dip-parallel outcrop photo of the Ketobe Knob thrust. The reconstruction of a balanced cross section is a common tool to validate an interpretation of structures in the field (Dahlstrom, 1969). While a restored cross section is a non-unique solution, through trial and error, a balanced restoration can reveal possible 1) fault nucleation locations, 2) fault propagation directions 3) the cause of fold formation, and 4) a possible order of events in the structure. We use these kinematic models which satisfy geometrical constraints, to motivate the finite element modeling. The methodology and results of the kinematic reconstructions are detailed in Wigginton (2018), and the geometry and kinematics of the structure are also described in Wacker, 2001; Souque et al., 2008; and Petrie et al., 2018.

We use the numerical finite element modeling program ABAQUS™ (Dassault Systèmes, 2011) to mechanically model fault-fold structures. This finite element code allows for the creation of complex geometries, including non-planar faults to be combined with mechanical stratigraphy and load conditions (Smart et al., 2009; Smart et al., 2012). The models satisfy the equilibrium, constitutive, and compatibility relationships necessary to create a mechanically permissible model. We establish the initial boundary conditions, stress state, and constitutive relationships, consider a range of material properties to simulate rock behavior (simple elastic or elastic-plastic responses) and examine variable friction between layers (Smart et al., 2008; 2012; Petrie and Evans, 2016). Parameterization studies were performed using a simple three layer model with a coarse mesh to test for model convergence, and to examine the impact of rock properties, interlayer slip, overburden pressure, fault friction, and fault angle individually. The preliminary models enabled us to decide on reasonable input values such as the use of damping factors, non-linear algorithms, and surface contact types (Smart et al., 2009, 2012; 2014). We then examined specific mechanical models with realistic stratigraphy and finer meshes in order to explore a range of questions, track the spatial and temporal distributions of magnitudes and orientations of stresses as well as elastic and inelastic strains throughout the model domain (Petrie and Evans, 2016; Smart et al., 2010, 2012). The finite element models have a rigid boundary condition at the base to prevent downward movement and a rigid boundary condition at the top to represent overburden material and to prevent excess distortion of the topmost layer (i.e., upward movement was restricted). These models do not incorporate pore pressure in the material properties.

The models consisted of two load steps. In step 1 we applied a downward gravitational acceleration to the model and let it equilibrate. The gravity load applied in step 1 remains on the model through step 2. In step 2 we applied the horizontal tectonic loads. The downward pressure simulates an overburden of 40 MPa as suggested from the stress orientation and magnitude inversions in 3D Stress from small fault slip data for the site (Souque et al., 2008; Morris, 2017; Wigginton, 2018). A horizontal load of 200 MPa is applied, which is more than sufficient to induce failure of all rock units in the model. Models were run with a range of mesh sizes and time increments to ensure we had achieved a convergent result - that is we tested to make sure that alteration of the time increment, and mesh size did not alter the distribution of stress and strain in the final model. We ran models with the same parameters and incrementally reduced the mesh size from 2 m to 0.5 m and altered the run time from 1 s to 10 s. Each model yielded the same pattern of stresses and very close to the same magnitudes.

RESULTS

Geologic Analyses

The Ketobe Knob thrust exposure is a lateral ramp in the southwestern part of the Buckhorn Flats thrust complex, in the Cedar Mountain thrust system, Utah (Figs. 2 and 3, Neuhauser et al., 1988; Wacker, 2001; Souque et al., 2008; Welch et al., 2009; Petrie et al., 2018) where moderate-displacement thrusts cut the Jurassic Entrada Formation through the Curtis Sandstone (Fig. 3). The following sections summarize the mechanical stratigraphy and cross section construction and restoration as published in Wigginton (2018).

Mechanical Stratigraphy

Rocks at the Ketobe Knob outcrop were divided into five mechanical units (Fig. 4; Table 1) based on the distribution of mesoscopic structures, mineralogic and sedimentary petrographic analyses, and Schmidt rebound hammer field tests (Wigginton, 2018). This mechanical stratigraphy is related to, but may differ from, formally recognized stratigraphic units. Relative rock strengths were determined in the field with an N-type Schmidt rebound hammer. Rebound was used with the following relationships to estimate UCS and E values:

$$\ln(\mathrm{UCS}) = 0.792 + 0.067R \tag{1}$$

$$\ln(E) = -8.967 + 3.091\ln(R) \tag{2}$$

where R = measured rebound value, E = Young's Modulus, and UCS is the uniaxial compressive (Aydin and Basu, 2005; Katz et al., 2000) (Table 1). The strongest units in the section are the sandstone-rich parts of the Entrada Formation, with E values of 17 to 22 MPa, and UCS values of 47 to 62 MPa, whereas the earthy Entrada, and the Curtis Formation rocks have values that are half these values (Table 1; Fig. 4). This meter-scale variation in elastic properties is consistent with the analyses of Petrie et al. (2012) and Petrie and Evans (2016) and these variations affect the brittle failure response of a layered sequence in a range of settings (Underwood and Cooke, 2003; Petrie et al., 2014). Mesoscopic structures include slickensides on bedding surfaces at the Ketobe Knob site, that indicate that interlayer frictional slip failure occurred during deformation throughout the area (Wigginton, 2018). Other mesoscopic structures include small folds and sheared rocks in shale-siltstone sequences, all of which indicate that the rocks deformed by brittle slip and shearing.

Cross Section Construction and Restoration

Wigginton (2018) generated restored cross sections in Move™ in which several variations of initial fault geometries and structural timing were explored and tested for acceptability by their area balance and logic of restorability. We created restorations from four different initial geometries because the highly deformed region in-between the upper and the lower fault left room for multiple interpretations (Wigginton, 2018). Over 20 restorations were attempted, a selection of which are presented in Wigginton (2018, Appendix B). With each of those initial geometries we varied the order of fault failure, location of fault nucleation, and the fault and fold algorithms applied. All attempted restorations, except our preferred interpretation, were considered unsuccessful due to the following problems: 1) the algorithms of the program could not complete an unfaulting or unfolding step (due to non-concentric folding) , or 2) they required steps which are not geologically reasonable, in that they created 1) more deformation than exists present day, 2) excessive layer thickening, or 3) unreasonably tight folding (Wigginton, 2018). Based on the detailed reconstruction steps (Wigginton, 2018, Appendix B), our preferred interpretation shows that the structures at the Ketobe Knob could reasonably be created by the series of events in Figure 5. It is also important to note that we do not assign a strict absolute timeline to the reconstruction; the faults and folds could have all formed in very short succession or simultaneously as connected relays.

The preferred area-balanced restoration (Fig. 5) consists of two sub-parallel thrust faults that nucleated in the sandstone member of the Entrada Formation and propagates upward and downward into the mechanically weaker rocks (made weaker due to laminations, less calcite cementation, or overall unit thickness (Wigginton, 2018)). The displacement-distance profile or displacement-distance diagram (Fig. 6) shows the likely region of fault nucleation could be the site with the greatest displacement (Muraoka and Kamata, 1983; Williams and Chapman, 1983; Ellis and Dunlap, 1988; Roche et al., 2012; Alsop et al., 2021). The lower fault shows the maximum displacement within f the upper sandstones of the Entrada Formation, and it loses displacement toward the upper and lower fault tips. This suggests that the fault nucleated in the upper Entrada Formation. Lastly, the upper fault shows a maximum displacement in the upper Entrada sandstone with less offset toward both fault tips. This profile suggests that the upper fault propagated upward and downward (Fig. 6).

Based on the preferred restoration we conclude that: (1) both major faults nucleated in mechanically strong upper sandstone of the Entrada Formation, (2) the upper and lower faults propagated upwards and downwards as shown by the decrease in displacement toward the upper and lower fault tips, and (3) the hanging-wall anticline and footwall syncline formed in mechanically weaker layers and were created by upward and downward fault propagation. While it is a non-unique solution, the successful reconstruction in *Move*™ supports a kinematic model in which the faults nucleate in structurally strong layers, propagate upwards and downwards, and create folds in more ductile stratigraphic units.

Mechanical Modeling

The finite element models of mechanically layered sequences in ABAQUS^{TM} explore the ramp-first style of thrust fault propagation. These models incorporate field data and provide a mechanically-based analysis of the development of the thrust faults at the Ketobe Knob site. We examine models for intact, unfaulted layered sequences with and without frictional interlayer slip (Fig. 7a), and models of a faulted layered sequence without and with variations of mechanical properties of the rock (Fig. 7b).

Model Inputs

Analysis of rock properties and the kinematic models of the Ketobe Knob site serves as the guide for the number of layers to include in the model, their thicknesses, compressive strengths, initial stress state of the model (Table 2), and the nature of interlayer slip. We use elastic–plastic (Mohr–Coulomb) material properties to describe the bulk deformation of upper crustal rocks (Smart et al., 2012), and use a Coulomb friction model to govern slip between layers and faulted surfaces (Smart et al., 2010).

We created two model suites within this framework: 1) intact and unfaulted models to examine how the difference in mechanical stratigraphy affects the distribution of stresses in the pre-faulted state, and 2) faulted models which use the same inputs but contain a planar fault (contact surface with a coefficient of friction) to show how a recently nucleated fault alters stress in the surrounding rocks. The faulted models were run with slight variations including a) variation in mechanical stratigraphy, b) uniform mechanical stratigraphy (no variation of strength between the layers), and c) variation in mechanical stratigraphy and deformed by a horizontal displacement load.

Unfaulted Models The unfaulted models provide the base case for the distribution of stresses and strains in an intact stratigraphic sequence. We apply horizontal far-field tectonic stresses to the strata and show how the difference in mechanical strength of each unit at the Ketobe Knob affects the distribution of stresses.

The unfaulted models reveal the dramatic variation of stresses that develop in different mechanical layers (Fig. 8a). The stresses in the modeled stratigraphic section range from ~130 MPain the weaker mechanical layers (representing properties derived from the Curtis sandstone, Curtis conglomerate, and Earthy Entrada silty member), and up to ~300 MPa in the strong mechanical layers (representing properties derived from sandstones in the Entrada Formation) (Fig. 8c). Animations of the model run show the stresses are consistently higher in the strong units (Table 1) and radiate outward through the weaker units (Wigginton, 2018). The largest contrast in layer strength is at the center of the model , and stress contrasts are pronounced at layer interfaces (Fig. 8c). A graph of stress through time (Fig. 9a) shows that during loading stresses in the mechanically layered sequence diverge rapidly with the higher stresses in strong units (Entrada sandstone) and the weaker units experience lower stresses. Graphs plotting stress vs strain show that the two strongest units (Table 1) are more resistant to deformation (i.e. for a given strain, stress is higher in the strong rock units; Fig. 8c). Stress-strain and stress-time curves (Fig. 9a and 9b) show that the weaker units depart from linear elastic behavior earlier than in the strong layer, and that ductile deformation continues through the model run.

Influence of Interlayer Slip We examine models where the coefficient of friction at layer interfaces varies from μ = 0.0 to 0.85. Smart et al. (2009) emphasizes the influence of interlayer slip on strain distributions in mechanically layered models. In the frictionless end member the layers freely slide past each other and stress magnitudes remain uniformly low through the sequence (Fig. 10a). Strain profiles (Fig. 10e) for this case shows that the free slip allows each layer to shorten independently and slip at their tops and bases (Fig. 10e). For the intermediate values of μ, the stresses are consistently higher in the strong units and radiate outward through the weaker units. As the values of the interlayer friction coefficients increase, the rock sequences exhibit reduced stresses in the Curtis Sandstone (Fig. 10), and significant increases in the stronger Entrada Sandstone. The strains are more uniformly distributed, whereas the stress distribution is heterogeneous (Figs. 10b-10d). The stresses in the stratigraphic section range from ~130 MPa to ~300 MPa. With μ of 0.85, the stresses in the stronger layers expand laterally, and are communicated broadly to the overlying layer (Fig. 10d).

The stress-time curves (Fig. 11) for these models provide insights into the behavior of the sequence. In the stress-time behavior for μ = 0 model, stresses in the strongest layer increase with time while all the other layers have similar, nearly linear stress-time behaviors. Towards the end of the simulation, stresses in the strong layer decrease, and the layer directly below exhibits an increase in stress, until at the end of the model run, all layers equilibrate to the same stress. Since each layer can respond independently during the model run, they develop their own strain behavior. As there is no bond strength with its overlying neighbors, the strongest layer does not effectively communicate any excess stress to the adjacent overlying layer. Some stresses are transferred to the lower layer, perhaps because the vertical loads are higher here. For any level of frictional strength between the layers, at the end of the model run stresses are concentrated in the strong layer and some of these stresses are transmitted to the vertically adjacent rocks.

Faulted Models

Due to the complexities in generating true shear fractures under compression in most finite element models (Hedayat et al., 2015; Zhuang et al., 2015; Sivakumar and Maji, 2016) we place a preexisting 20° dipping fault to represent a nascent thrust fault in the Entrada Formation where stresses in the unfaulted model are highest (Fig. 11). The fault is formed by a contact surface with a coefficient of friction between two elements with material properties of the Entrada Sandstone. We examine models in which: a) there are variations in mechanical stratigraphy and the rocks are deformed by a stress boundary condition load, b) there is no variation in mechanical stratigraphy and the rocks are deformed by a stress boundary condition, and c) variations in mechanical stratigraphy are present and the section is deformed by a displacement boundary condition. The model parameters (material properties of the units, boundary conditions, and loading conditions) for the faulted models are the same as for the unfaulted models (Tables 3 and 4).

No Variation in Mechanical Stratigraphy The model of a newly formed thrust fault in uniform mechanical stratigraphy is the base case for the faulted models and shows the distribution and concentrations of stresses created by a newly formed fault without the additional impact of mechanically layered stratigraphy. All the model inputs remain the same as the previous model, except that we assign uniform material properties (those used to represent the upper Entrada sandstone) to represent a layered, mechanically uniform package of sedimentary rocks (Fig. 12).

Both fault tips show Coulomb stress perturbations with a stress increase in the compressional quadrants, a very focused stress increase at the footwall of the upper fault tip, and corresponding decreases in stress in the dilatational quadrants (Fig. 12). The hanging wall above the upper fault tip and below the lower fault tip both show an increase in stress and heterogeneous reorientation of stress axes around the fault tips (Fig. 12b). The region of increased stress below the lower fault tip is larger than the area of increased stress above the upper fault tip (Fig. 12). This result shows that without the added effect of mechanical stratigraphy, nascent thrust faults may result in increased stress increases near the faults tips and this induces deformation in the hanging wall and footwall near the fault tips. Stress magnitudes are slightly larger in the strongest units (Table 1) throughout the simulation.

Models with Variation in Mechanical Stratigraphy The faulted model with variation in mechanical stratigraphy, based on the mechanical stratigraphy at the Ketobe Knob, shows an extreme concentration of elevated maximum principal compressive stress magnitude at the fault tips and in the footwall and hanging wall wedges (Figs. 13 and 14). High compressive stresses form in the hanging wall and footwall wedges first, then radiate outward through the rest of the model.

The compressive stresses are also consistently elevated in the units above (Curtis Conglomerate) and below (earthy Entrada Sandstone) the fault tips. Stresses in the stratigraphic units above and below the strong layers are significantly lower. There is a larger increase of stress in the footwall than in the hanging wall. Cumulative strain is extremely high in the Curtis conglomerate and earthy Entrada sandstone directly adjacent to the fault tips (Fig. 13). The patterns of elevated strain show the same vergence directions of the folds at the Ketobe Knob outcrop; the strain pattern for the hanging wall anticline verges to the right, and the strain pattern for the footwall syncline verges to the left.

Models with Variation in Mechanical Stratigraphy and a Displacement Boundary Condition The displacement model simulates a rapid loading scenario (Smart et al., 2010, 2012). This model shows the perturbed stress state directly after the loading event (Fig. 13). The displacement boundary condition necessitates additional material be added to the edges of the model to absorb material failure directly adjacent to the applied load. We add a thick base layer for the upper units to slide over to avoid edge effects of the lower boundary condition. The displacement load model parameters (Table 4) have an initial static stress state to create a pre-stressed volume of rock in a contractional stress regime. The gravitational load is applied in step 1. In step 2 an additional boundary condition is placed on the right side of the model to prevent movement in the x direction, then a horizontal displacement of 2 m was applied to the left side (Fig. 15a). The displacement models use the same material properties as previous versions except for the interlayer slip and fault coefficient of friction (Table 4). We applied a friction coefficient of μ = 0.2 to layer contacts to allow interlayer slip and prevent the layers from failing where the load was applied.

Faulted models deformed by the displacement boundary condition facilitate more deformation in the form of folds and result in significant stress concentrations and principal stress reorientations at fault tips (Fig. 15). We apply 2 m of horizontal displacement to the hanging wall. The results show the units above and below the fault are deformed into fault propagation folds (Fig. 15). A hanging wall anticline in the Curtis conglomerate model layer, and a footwall syncline in the earthy Entrada silty sandstone model layers developed. The hanging wall anticline verges to the right and the footwall syncline verges to the left. The footwall syncline (5.5 m amplitude) is larger than the hanging wall anticline (2.7 m amplitude). This difference in fold amplitude could be due to the differences in bed thickness of the modeled Curtis conglomerate and the earthy Entrada sandstone, differences in material properties, or the increase in overburden pressure at the lower fault tip (Fig. 15). Animations of the model show simultaneous formation of the hanging wall anticline and footwall syncline as displacement increases on the fault. The distribution of stresses in the model also indicates that the formation of a back-thrust in the Curtis sandstone (Fig. 15b). The stress pattern shows a thin band of increased stress at ~40°. High stress concentrations on the left side of the model should be disregarded as they are a result of rock failure at the location of load application. The distribution of stresses in each unit through time (Fig. 16) mirrors results from the unfaulted model before they level off later in the loading step (Fig. 11). Stresses are highest in the Entrada sandstone units and lower in the Curtis Formation and the earthy Entrada, as seen in all previous models.

The extreme stress concentration at the hanging wall side of the lower fault tip (Fig. 15d) exhibits the geometry of a back thrust at the lower fault tip. Principal stress orientations are significantly reoriented here. These orientations indicate that steeply dipping faults would form at the lower tip zones of the faults (see also Strayer and Hudleston, 1997).

DISCUSSION

The results of the finite element models based on field data and kinematic restorations provide insights into how the mechanical stratigraphy of rocks influences thrust fault nucleation and propagation, and we examine the ramp-first model for thrust fault development (Eisenstadt and De Paor, 1987; Ferrill et al., 2016; Alsop et al., 2021). We discuss the nature of the fault-to-fold transitions, the nature of mechanical stratigraphy and its influence on the structure, and details of the fault development.

Mechanical Stratigraphy

A number of factors contribute to determining how layered rocks respond to stresses including primary rock textures and diagenetic or metamorphic processes. Rock composition may significantly affect failure properties, but there are few universal relationships solely between lithology and rock strength in many clastic sedimentary rocks (Busetti and Fang, 2018). Instead, lithology combined with layer thicknesses, grain size, grain composition, laminae, degree and nature of cementation, burial history, and other factors affect rock strength and failure modes in these types of rocks (Corbett et al., 1987; Petrie et al., 2015; Busetti and Fang, 2018).

The numerical modeling results (Figs. 8-16) show that the stress magnitudes are significantly perturbed from the uniform starting stresses in all models in response to horizontal shortening. Peak stresses are larger in the stronger horizons, whereas the weaker units have much lower stresses. The models show that the uniform stress state at the beginning of the model runs quickly deviate to produce nonuniform distributions. We also show how to use experimentally determined rock mechanics properties for the rocks exposed at Ketobe Knob in conjunction with basic Mohr-Coulomb failure analysis to show how failure might first occur in these stronger horizons (Petrie et al., 2015). Experimentally determined values for the cohesive strengths and tensile strengths of similar rocks (Petrie et al., 2014; Petrie et al., 2015) provide general constraints on the Coulomb failure envelopes in these rocks. The relatively strong Entrada Sandstone sequences tend to have lower tensile strength and higher cohesive strength than the silt-rich rocks. At the differential stresses predicted in our models, the Entrada Sandstone layers are likely to reach failure (Fig. 17). In contrast, the low stresses in the weaker rocks, combined with slightly higher tensile strengths, indicate that the weaker rocks (as determined by field measurements) may not reach failure (Fig. 17). While the yield strengths of the weak rocks are lower, the stresses in the weak rocks are also significantly reduced as the strong rocks act as a load bearing sequence. This stress imbalance and strength difference within the mechanically layered stratigraphic section reverses the anticipated order of rock failure. We note that the range of yield strengths measured at the surface may differ from the rock properties at depth. We model faulting at the overburden load of 2 km, which corresponds to the maximum burial of the rocks, and during the time frame inferred for deformation of these rocks (Neuhauser et al., 1988). he differences in mechanical strength may have been less extreme at depth, thereby dampening the observed stress partitioning in response to an applied horizontal compressive stress. However, the analyses of variations of frictional properties are sound regardless of the burial history, and the results in the mechanically layered sequence provide insight into the relative behavior of the rocks.

The strength contrast between units affects fracture propagation (Petrie, 2014). Two rock units with similar strengths are likely to have a fracture propagate through the interface. Conversely, strong layer contrasts (a weak unit next to a strong unit) are likely to arrest propagating fractures (Cooke and Underwood, 2001; Larsen et al., 2010). This relationship is demonstrated by the fault and fold formation at the Ketobe Knob where faults likely nucleated in stiff units, then formed fault propagation folds in more ductile units before they broke through.

Mechanics of Thrust Fault Development

The finite element models provide a mechanical explanation for the field observations and reconstructions of the thrust fault-fold relationships (Ferrill et al., 2016; Wigginton, 2018). The results from the faulted models show that initially uniform stresses in the sedimentary rocks quickly evolve to non-uniform distributions with high stresses concentrated in the strong layers. In the faulted models, stress becomes concentrated at fault tips in the upper and lower weaker layers (Eisenstadt and De Paor, 1987), and conjugate stresses form from the lower fault tip. Fault-propagation folds form and the faulted models show an increase in stress and strain in the unfaulted units around the fault tips (in the Curtis conglomerate and the Earthy Entrada). While the fold amplitudes are not the same as the folds seen in the field, it is easy to imagine that this model is an early snapshot in the formation history of the present-day structures at the Ketobe Knob. The increase in stress occurred in the models without variation in mechanical stratigraphy and are even more dramatic in the models with variation in mechanical stratigraphy (stress in the strong layers is more than twice the stress in the weak layers). The results also explain macroscale footwall folding that is so common; the stress and strain heterogeneities are present at both the upper and lower fault tips regardless of the direction of propagation or the mechanical stratigraphy.

The development of a high stress region in the hanging wall of the thrust, near its upper fault tip, and dipping towards the fault predicts that significant deformation should occur in the hanging wall of the thrust (Fig. 13). The stress patterns are similar to the back thrust development predicted from rock models (Morse, 1977; Chester et al. 1991; Marshak et al., 2019), analytical models (Berger and Johnson, 1982; Kilsdonk and Fletcher, 1989), field studies (Serra, 1977; McConnell et al., 1997), and kinematic models (Welch et al., 2009). Our results also suggest that high back-thrust stresses develop early in the junction of the fault tip and the lower, weaker rock contact, consistent with analog models of frontal thrust development (Morse, 1977; Marshak et al., 2019).

We based our models on mechanical stratigraphy that is distilled from the field-based measurements, and considered a single fault. This ensures that we produced tractable models that evaluated the impact of mechanical stratigraphy and rock properties on stress distributions at fault tips. The Ketobe Knob thrust consists of several faults (Figure 3) and the mechanical stratigraphy may have affected how these faults interacted as the structure evolved. Such complexity may warrant further analyses.

Fold Geometry

The Ketobe Knob thrust faults and associated hanging wall anticlines and footwall synclines reveal fault/fold geometries that are compatible with the ramp-first style of thrust fault formation. The presence of macroscale footwall deformation at the Ketobe Knob (Wigginton 2018; Petrie et al.et al., 2018) and in other studies (McConnell et al., 1997; Ferrill et al., 2017) favor ramp-first formation over flat-ramp formation. The Ketobe Knob thrust shape and position of the folds are consistent with that expected from fault propagation folds, i.e. when the fault propagates through the fault tip folds it leaves behind tight, steep to overturned anticlines and synclines adjacent to the fault surface (Suppe and Medwedeff, 1990). The elevated stress and heterogeneous reorientation of stress axes at the upper and lower fault tips in faulted models agree with analogue and analytical models (Rodgers and Rizer, 1981; Patton and Fletcher, 1995). The region of potential failure (folding) directly above a reverse-fault is elongated parallel to the dip of the fault (Patton and Fletcher, 1995). . Rodgers and Rizer (1981) found shear stress to be the greatest at the fault tip and vertical displacement increased above the fault tip. These results and our results enforce the concept that elevated stresses may generate fault propagation folds at fault tips, regardless of lithology or propagation direction.

The folded Curtis conglomerate and Earthy Entrada silty sandstone exhibit thinner beds than the other units. The Curtis conglomerate is only 1.6 m thick and the Earthy Entrada unit is 2.9 m thick but contains extremely fine laminations (0.25 mm in thin section). The Curtis sandstone, while weaker in terms of elastic strength (low rebound) is very thickly bedded, which explains its lack of folds in the hanging wall. The upper and lower Entrada sandstones are elastically strong (high rebound) and are thickly bedded, which would make them the most competent units in the stratigraphic section. Analytical mechanical models of free slip along fault ramps (Kilsdonk and Fletcher, 1989) predict that a footwall ramp syncline may result in cases where the footwall is stiffer than the hanging wall, with thinning and extension of the footwall. Our models do not allow for free slip, and the fault tips are “pinned”. Evolution of the structures from pinned to free slip may result in changes from contractional to extensional strains in the fault tip – fault ramp regions.

The sizable amplitude difference between the hanging wall anticline and footwall syncline could be due to textural differences in the rocks (i.e. the degree of cementation and the thickness of bedding/laminations). The Earthy Entrada silty sandstone is weakly cemented, very finely laminated, and has smaller grain size which make it more ductile. Conversely, the Curtis conglomerate contains thicker beds, larger grain sizes, and strong cementation, making it less ductile than the Earthy Entrada. A propagating thrust fault may be impeded for longer (creating a larger amplitude fault propagation fold) in the more ductile of the two units.

These results shed light on the mechanics of thrust fault formation of a range of scales beyond that of the Ketobe Knob and other outcrop-scale structures (McConnell et al., 1997; Marshak et al., 2019, their Fig. 11). Thrust faults that form in the ramp-first faulting style are observed in the foreland of large thrust belts, including the Canadian Rockies (Link, 1949; Teal, 1983; Morley, 1994; Begin et al., 1996; McMechan, 1999; Langenberg et al., 2006), the Osen-Røa thrust sheet in Norway (Morley, 1994), and the Wyoming thrust belt (Woodward, 1986; Fischer et al., 1992). Sometimes called “sled runners” or “incipient thrusts”, small-displacement thrusts form 10’s of km in front of the conventionally defined fold and thrust belt (McMechan, 1999). In seismic reflection profiles these faults appear to cut stiff sandstone units and lose displacement above and below in weaker reflectors (Teal, 1983; McMechan, 1999).

CONCLUSIONS

We integrate traditional structural geology field methods, 2-dimensional cross section reconstructions, and finite element mechanical models to investigate the effects of mechanical stratigraphy on stress heterogeneity, rupture direction, and fault geometry by examining a large-scale field example of ramp-first faulting in central Utah. The results of this study provide strong support for the importance of the ramp-first faulting style in mechanically stratified systems. The mechanical stratigraphy of faulted rocks exerts a first-order control on thrust fault formation. Kinematic reconstructions and finite element models indicate that faults at the Ketobe Knob nucleated in structurally strong (stiff, low ductility) layers, then propagated upward and downward, and created fault propagation folds at both fault tips. Numerical models provided a mechanical explanation for the kinematics; strong rock units showed elevated stresses and more brittle behavior making them likely to fault first. Weak units showed lower stresses, but were more likely to respond ductilely and form folds under pressure. When a fault was nucleated in the layered system, the finite element models showed similar fold orientations to those seen in the outcrop.

We hypothesize that in some cases thrust fault nucleation occurs in the ramp-first style that then evolves to ramps that are linked by flats (slip along long angle, weak surfaces) (Eisenstadt and De Paor, 1987; Marshak et al., 2019). Many thrust systems may originate in this way, but field evidence is hard to unravel due to the overprinting by later deformation. Because we rarely see complete thrust faults in the field from upper fault tip to lower fault tip, identifying large ramp-first faults in the field is not straightforward. However, stratigraphy, the position and shape of flanking folds, fault-displacement profiles, and balanced cross section restorations can provide clues to kinematics. This study emphasizes the importance of incorporating mechanics and knowledge of lithology into cross section restorations and the study of thrust fault kinematics.

Acknowledgements: Funding for the support for Sarah Wigginton MSc. research includes grants from the GDL Foundation, the Utah State University Graduate Research and Collaborative Opportunities program, Geological Society of America, the American Association of Petroleum Geologists, the Salt Lake City chapter of The Association of Women Geologists, and the Utah State University Geosciences Department J. S. Williams endowment. Academic discounts and access to Move™ and ABAQUS™ software are gratefully acknowledged. Many thanks to Kevin J. Smart for guidance on finite element modeling, to Russell Davies, Raymond Fletcher, and Sandro Serra for comments on an earlier draft of this paper, and to journal reviews David Ferrill and Vincent Roche for insightful reviews.

REFERENCES

Apotria, T.G., and Wilkerson, M.S., 2002, Seismic expression and kinematics of a fault related fold termination: Rosario structure, Maracaibo Basin, Venezuela: Journal of Structural Geology, v. 24, p.671–687. DOI: 10.1016/s0191-8141(01)00123-7

Aydin, A., and Basu, A., 2005, The Schmidt hammer in rock material characterization: Engineering Geology, v. 81, p. 1–14, DOI:10.1016/j.enggeo.2005.06.006.

Begin, N.J., Lawton, D.C., and Spratt, D.A., 1996, Seismic interpretation of the Rocky Mountain Thrust Front near the Crowsnest Deflection, Southern Alberta: Bulletin of Canadian Petroleum Geology, v. 44, p. 1–13, DOI:10.2113/gscpgbull.56.3.199.

Berger, P., and Johnson, A. M., 1982, Folding of passive layers and forms of minor structures near terminations of blind thrust faults – application to the central Appalachian blind thrust: Journal of Structural Geology, v. 4, p. 343-353. https://doi.org/10.1016/0191-8141(82)90018-9.

Bourne, S.J., 2003, Contrast of elastic properties between rock layers as a mechanism for the initiation and orientation of tensile failure under uniform remote compression: Journal of Geophysical Research: Solid Earth, v. 108, p. 2580–2600, DOI: 10.1029/2001JB001725.

Boyer, S.E., and Elliott, D., 1982, Thrust systems: American Association of Petroleum Geologists Bulletin, v. 66, p. 1196–1230. https://doi.org/10.1306/03b5a77d-16d1-11d7-8645000102c1865d

Bracken, K .A., 2020, Mechanical stratigraphy and layer-bound normal faulting in the Upper Cretaceous Niobrara Formation, Wattenberg Field, Colorado: The Mountain Geologist, v.57, p. 67-94. https://doi.org/10.31582/rmag.mg.57.2.67

Busetti, S., and Fang, Z., 2018, Lithologic controls on shale rheology: A lookback on 7 years of mechanical testing: American Association of Petroleum Geologists Datapages/Search and Discovery, Article #90323.

Butler, R.W.H., 1982, The terminology of structures in thrust belts: Journal of Structural Geology, v. 4, p. 239–245, DOI: 10.1016/0191-8141(82)90011-6.

Byerlee, J.D., 1978, Friction of Rocks: Birkhäuser, Basel, v. 116, p. 615–626, https://doi.org/10.1007/BF00876528.

Cawood, A. J., and Bond, C. E., 2020, Broadhaven revisited: a new look at models of fault–fold interaction, in: Bond, C. E. & Lebit, H. D. (eds.) Folding and Fracturing of Rocks: 50 Years of Research since the Seminal Text Book of J. G. Ramsay. Geological Society, London, Special Publications, 487, 105–126, https://doi.org/10.1144/SP487.11.

Chapman, T.J., and Williams, G.D., 1985, Strains developed in the hanging walls of thrusts due to their slip/propagation rate: a dislocation model: reply: Journal of Structural Geology, v. 7, p. 759–762, DOI: 10.1016/0191-8141(85)90152-X.

Chester, J.S., 2003, Mechanical stratigraphy and fault–fold interaction, Absaroka thrust sheet, Salt River Range, Wyoming: Journal of Structural Geology, v. 25, p. 1171–1192, DOI: 10.1016/S0191-8141(02)00151-7.

Chester, J.S., Logan, J.M., and Spang, J., 1991, Influence of layering and boundary conditions on fault-bend and fault-propagation folding, Geological Society of America Bulletin v. 103, p. 1059-1072, https://doi.org/10.1130/0016-7606(1991)103<1059:IOLABC>2.3.CO;2.

Cooke, M.L., and Underwood, C.A., 2001, Fracture termination and step-over at bedding interfaces due to frictional slip and interface opening: Journal of Structural Geology, v. 23, p. 223–238, DOI: 10.1016/S0191-8141(00)00092-4.

Cooper, M.A., and Trayner, P.M., 1986, Thrust-surface geometry: implications for thrust-belt evolution and section-balancing techniques: Journal of Structural Geology, v. 8, p. 305–312,: 10.1016/0191-8141(86)90051-9.

Corbett, K, Friedman, M., and Spang, J. 1987, Fracture development and mechanical stratigraphy of Austin Chalk, Texas: American Association of Geologists Bulletin, v. 71, p.17-28, https://doi.org/10.1306/94886D35-1704-11D7-8645000102C1865D.

Currie, J.B., Patnode, H.W., and Trump, R.P., 1962, Development of folds in sedimentary strata: Geological Society of America Bulletin, v. 73, p. 655–673, doi: 10.1130/0016-7606(1962)73[655:DOFISS]2.0.CO;2.

Dahlstrom, C.D.A., 1970, Structural geology in the eastern margin of the Canadian Rocky Mountains: Bulletin of Canadian Petroleum Geology, v. 18, p. 332–406, DOI:10.1306/5D25CA81-16C1-11D7-8645000102C1865D.

Dassault Systèmes, 2016, ABAQUS® User Manual, SIMULIA, a division of Dassault Systèmes, Providence, Rhode Island:, http://130.149.89.49:2080/v2016/books/usb/default.htm?startat=pt04ch10s07at36.html#usb-anl-aenrichment.

Doelling, H.H., Kuehne, P.A., Willis, G.C., and Ehler, J.B., 2015, 1:100,000 scale Geologic map of the San Rafael Desert 30’ x 60’ quadrangle, Emery and Grand Counties, Utah: Utah Geological Survey.

Eisenstadt, G., and De Paor, D.G., 1987, Alternative model of thrust-fault propagation: Geology, v. 15, p. 630–633, DOI: 10.1130/0091-7613(1987)15<630:AMOTP>2.0.CO;2.

Ellis, M.A., and Dunlap, W.J., 1988, Displacement variation along thrust faults: implications for the development of large faults: Journal of Structural Geology, v. 10, p. 183–192, DOI: 10.1016/0191-8141(88)90115-0.

Erickson, G.S., 1996, Influence of mechanical stratigraphy on folding vs. faulting: Journal of Structural Geology, v. 18, p. 443–450, DOI: 10.1016/0191-8141(95)00064-K.

Ferrill, D.A., and Morris, A.P., 2008, Fault zone deformation controlled by carbonate mechanical stratigraphy, Balcones fault system, Texas: American Association of Petroleum Geologists Bulletin, v. 92, p. 359–380, DOI: 10.1306/10290707066.

Ferrill, D.A., Morris, A.P., McGinnis, R.N., Smart, K.J., Wigginton, S.S., and Hill, N.J., 2017, Mechanical stratigraphy and normal faulting: Journal of Structural Geology, v. 94, p. 275–302, DOI: 10.1016/j.jsg.2016.11.010.

Ferrill, D.A., Morris, A.P., Wigginton, S.S., Smart, K.J., McGinnis, R.N., and Lehrmann, D., 2016, Deciphering thrust fault nucleation and propagation and the importance of footwall synclines: Journal of Structural Geology, v. 85, p. 1–11, DOI: 10.1016/j.jsg.2016.01.009.

Fischer, M.P., and Jackson, P.B., 1999, Stratigraphic controls on deformation patterns in fault-related folds: a detachment fold example from the Sierra Madre Oriental, northeast Mexico: Journal of Structural Geology, v. 21, p. 613–633, DOI: 10.1016/S0191-8141(99)00044-9.

Fischer, M.P., Woodward, N.B., Mitchell, M.M., 1992, The kinematics of break-thrust folds: Journal of Structural Geology, v. 14, p. 451-460, https://doi.org/10.1016/0191-8141(92)90105-6.

Gercek, H., 2007, Poisson’s ratio values for rocks: International Journal of Rock Mechanics and Mining Sciences, v. 44, p. 1–13, DOI: 10.1016/j.ijrmms.2006.04.011.

Goodman, R.E., 1980, Introduction to Rock Mechanics: Wiley, 582 p, ISBN: 978-0-471-81200-5.

Grasemann, B., Martel, S., and Passchier, C., 2005, Reverse and normal drag along a fault: Journal of Structural Geology, v. 27, p. 999–1010, DOI: 10.1016/j.jsg.2005.04.006.

Grasemann, B., Stüwe, K., and Vannay, J.-C., 2003, Sense and non-sense of shear in flanking structures: Journal of Structural Geology, v. 25, p. 19–34, DOI: 10.1016/S0191-8141(02)00012-3.

Gross, M.R., Fischer, M.P., Engelder, T., and Greenfield, R.J., 1995, Factors controlling joint spacing in interbedded sedimentary rocks: integrating numerical models with field observations from the Monterey Formation, USA: Geological Society, London, Special Publications, v. 92, p. 215–233, DOI: 10.1144/GSL.SP.1995.092.01.12.

Gutiérrez-Alonso, G., and Gross, M.R., 1999, Structures and mechanisms associated with development of a fold in the Cantabrian Zone thrust belt, NW Spain: Journal of Structural Geology, v. 21, p. 653–670, DOI: 10.1016/S0191-8141(99)00055-3.

Hart, B.S. and Cooper, S., 2021, Mechanical stratigraphy in Mesozoic rocks of the San Juan Basin: Integration of stratigraphic and structural terms and concepts: The Mountain Geologist, v. 59, p. 159-204, DOI: 10.31582/rmag.mg.58.2.159.

Hedayat, A., Ochoa-Cornejo, F., and Khasawneh, Y., 2015, Numerical simulation of crack initiation and growth in rock specimens containing a flaw under uniaxial compression, *in* Conference: 49th US Rock Mechanics/Geomechanics Symposium, San Francisco, CA, USA.

Hughes, A.N., Benesh, N.P., and Shaw, J.H., 2014, Factors that control the development of fault-bend versus fault-propagation folds: Insights from mechanical models based on the discrete element method (DEM): Journal of Structural Geology, v. 68, p. 121–141, DOI: 10.1016/j.jsg.2014.09.009.

Hughes, A.N., and Shaw, J.H., 2014, Fault displacement-distance relationships as indicators of contractional fault-related folding style: American Association of Petroleum Geologists Bulletin, v. 98, p. 227-251. DOI:10.1306/05311312006.

Hughes, A.N., and Shaw, J.H., 2015, Insights into the mechanics of fault-propagation folding styles: Geological Society of America Bulletin, v. 127, p. 1752–1765, DOI: 10.1130/B31215.1.

Katz, O., Reches, Z., and Roegiers, J.C., 2000, Evaluation of mechanical rock properties using a Schmidt Hammer: v. 37, p. 723–728, DOI: doi.org/10.1016/S1365-1609(00)00004-6.

Kilsdonk, B., and Fletcher, R.C., 1989, An analytical model of hanging-wall and footwall deformation at ramps on normal and thrust faults: Tectonophysics, v. 163, p. 153-168,https://doi.org/10.1016/0040-1951(89)90123-6.

Koyi, H.A., and Teixell, A., 1999, Where is the footwall flat? A cautionary note on template constraints: Journal of Structural Geology, v. 21, p. 373–377, DOI: 10.1016/S0191-8141(99)00009-7.

Langenberg, C.W., Beaton, A., and Berhane, H., 2006, Regional evaluation of the coalbed-methane potential of the Foothills/Mountains of Alberta, Canada: International Journal of Coal Geology, v. 65, p. 114–128, DOI: 10.1016/j.coal.2005.04.010.

Larsen, E.B., 2015, Geomechanical and Structural characteristics of a paleoreservoir-caprock succession; sandstones of Humbug Flats, Central Utah, Master's Thesis: University of Oslo.

Larsen, B., Grunnaleite, I., and Gudmundsson, A., 2010, How fracture systems affect permeability development in shallow-water carbonate rocks: An example from the Gargano Peninsula, Italy: Journal of Structural Geology, v. 32, p. 1212–1230, DOI: 10.1016/j.jsg.2009.05.009.

Laubach, S.E., Olson, J.E., and Gross, M.R., 2009, Mechanical and fracture stratigraphy: American Association of Petroleum Geologists Bulletin, v. 93, p. 1413–1426, DOI: 10.1306/07270909094.

Marshak, S., Haqb, S. S. B., Sen, P., 2019, Ramp initiation in fold-thrust belts: Insight from PIV analysis of sandbox models: Journal of Structural Geology, v. 118, p. 308-323, DOI:10.1016/j.jsg.2018.11.006.

McClay, K.R. (Ed.), 1992, *Thrust Tectonics*: Dordrecht, Springer Netherlands, DOI: 10.1007/978-94-011-3066-0.

McClay, K. R., 2011, Introduction to Thrust Fault-related Folding, in: McClay, K. R., Shaw, J. H., & Suppe, J. eds., *Thrust fault-related folding*. Tulsa, OK: American Association of Petroleum Geologists Memoir 94, p. 1-21, DOI:https://doi.org/10.1306/13251330M9450.

McConnell, D.A., Kattenhorn, S.A., and Benner, L.M., 1997, Distribution of fault slip in outcrop-scale fault-related folds, Appalachian Mountains: Journal of Structural Geology, v. 19, p. 257–267, DOI: doi.org/10.1016/S0191-8141(96)00094-6.

McGinnis, R.N., Ferrill, D.A., Morris, A.P., Smart, K.J., and Lehrmann, D., 2017, Mechanical stratigraphic controls on natural fracture spacing and penetration: Journal of Structural Geology, v. 95, p. 160–170, DOI: 10.1016/j.jsg.2017.01.001.

McMechan, M.E., 1999, Geometry of the Structural Front in the Kakwa Area, Northern Foothills of Alberta: Bulletin of Canadian Petroleum Geology, v. 47, p. 31–42, DOI:10.35767/gscpgbull.47.1.031.

Mitra, S. 1990, Fault-propagation folds: Geometry, kinematic evolution, and hydrocarbon traps: American Association of Petroleum Geologists Bulletin, v. 74, p. 921-945.

Mitra, S., and Mount, V.S., 1998, Foreland Basement-Involved Structures: American Association of Petroleum Geologists Bulletin, v. 82, p. 70–109, DOI: 10.1306/1D9BC39F-172D-11D7-8645000102C1865D.

Morley, C.K., 1994, Fold-generated imbricates: examples from the Caledonides of Southern Norway: Journal of Structural Geology, v. 16, p. 619–631, DOI:https://doi.org/10.1016/0191-8141(94)90114-7.

Morris, A.P., 2017, 3DStress® Geological Software: Southwest Research Institute, https://www.swri.org/3dstress-geology-software (accessed May 2018).

Morse, J., 1977, Deformation in ramp regions of overthrust faults: Experiments with small-scale rock models, in: Heisey, E. L., Lawson, D. E., Norwood, E. R., Wach, P. H., Hale, L. A. [eds.] , Rocky Mountain Thrust Belt, Geology and Resources, Wyoming Geological Association Guidebook 28, p. 457-470.

Muraoka, H., and Kamata, H., 1983, Displacement distribution along minor fault traces: Journal of Structural Geology, v. 5, p. 483–495, DOI: 10.1016/0191-8141(83)90054-8.

Neuhauser, K.R., 1988, Sevier-age ramp-style thrust faults at Cedar Mountain, northwestern San Rafael Swell (Colorado Plateau), Emery County, Utah: Geology, v. 16, p. 299–302, DOI: 10.1130/0091-7613(1988)016<0299:SARSTF>2.3.CO;2.

Newson, A.C., 2015, Imaging the overturned limb of a footwall syncline and its impact on exploration in fold and thrust belts: Recorder, Canadian Society of Exploration Geophysicists, v. 40.

Odonne, F., 1990, The control of deformation intensity around a fault: natural and experimental examples: Journal of Structural Geology, v. 12, p. 911–921, DOI: 10.1016/0191-8141(90)90064-6.

Patton, T.L., and Fletcher, R.C., 1995, Mathematical block-motion model for deformation of a layer above a buried fault of arbitrary dip and sense of slip: Journal of Structural Geology, v. 17, p. 1455–1472, DOI: 10.1016/0191-8141(95)00034-B.

Petroleum Experts, https://www.petex.com, “MOVE Core Application”.

Petrie, E. S., Sundal, A. J., Wigginton, S. S., and Evans, J. P., 2018, Damage Zone Structure and Structural Diagenesis Associated with Thrust Faults – Emery County, Utah, American Association Petroleum Geologists, Annual meeting, Salt Lake City, Utah, Search and Discovery Article #51520, DOI:10.1306/51520Petrie2018. https://www.searchanddiscovery.com/documents/2019/51520petrie/ndx_petrie.pdf.

Petrie, E.S., and Evans, J.P., 2016, Modeling strain across mechanical sedimentary lithologic interfaces: geomechanical models derived from outcrop analysis: Bulletin of Canadian Petroleum Geology, v. 64, p. 477–494, DOI: 10.2113/gscpgbull.64.4.477.

Petrie, E.S., Evans, J.P. and Bauer, S.J., 2014, Failure of cap-rock seals as determined from mechanical stratigraphy, stress history, and tensile-failure analysis of exhumed analogs: American Association of Petroleum Geologists Bulletin v. 98, p. 2365-2389.DOI:10.1306/06171413126

Petrie, E.S., Evans, J.P. and Bauer, S.J., 2015, Determining the effect mechanical rock properties have on variability in fracture gradients, AAPG Datapages/Search and Discovery Article #90216, AAPG Annual Convention and Exhibition, Denver, CO.

Petrie, E.S., Jeppson, T.N., and Evans, J.P., 2012, Predicting rock strength variability across stratigraphic interfaces in caprock lithologies at depth: Correlation between outcrop and subsurface: Environmental Geosciences, v. 19, p. 125-142. DOI:10.1306/eg.06011212001

Ramsay, J.G., 1992, Some geometric problems of ramp-flat thrust models, *in* McClay K.R. (ed.) Thrust Tectonics. Springer, Dordrecht, p. 191–200, DOI:10.1007/978-94-011-3066-0_17.

Reches, Z., and Eidelman, A., 1995, Drag along faults: Tectonophysics, v. 247, p. 145–156, DOI: 10.1016/0040-1951(94)00170-E.

Roche, V., Homberg, C., and Rocher, M., 2012, Fault displacement profiles in multilayer systems: from fault restriction to fault propagation, Terra Nova, v. 24, p. 499–504, https://doi.org/10.1111/j.1365-3121.2012.01088.x.

Roche, V., Homberg, C., and Rocher, M., 2013, Fault nucleation, restriction, and aspect ratio in layered sections: Quantification of the strength and stiffness roles using numerical modeling: Fault modeling in layered sections: Journal of Geophysical Research: Solid Earth, v. 118, p. 4446–4460, DOI: 10.1002/jgrb.50279.

Rodgers, D.A., and Rizer, W.D., 1981, Deformation and secondary faulting near the leading edge of a thrust fault: Geological Society, London, Special Publications, v. 9, p. 65–77, DOI: 10.1144/GSL.SP.1981.009.01.07.

Schmidt, C. J., Evans, J. P., Harlan, S. S., Weberg, E. D., Brown, J. S., Batatian, D., Derr, D. N., Malizzi, L., McDowell, R. J., Nelson, G. C., Parke, M., and Genovese, P. W., 1993, Mechanical behavior of basement rocks during movement of the Scarface thrust, central Madison Range, Montana, in: Schmidt, C. J., Chase, R. B., and Erslev, E.A., eds., Laramide Basement Deformation in the Rocky Mountain Foreland of the Western United States, Geological Society of America Special Paper 280, p. 89-106, DOI:10.1130/SPE280-p89.

Serra, S., 1977, Styles of deformation in the ramp regions of overthrust faults, in: Heisey, E. L., Lawson, D. E., Norwood, E. R., Wach, P. H., Hale, L. A. [eds.] Rocky Mountain Thrust Belt, Geology and Resources, Wyoming Geological Association Guidebook 28, p. 487-498.

Sivakumar, G., and Maji, V.B., 2016, Simulation of crack propagation in rocks by XFEM, Advances in Engineering Research, DOII: 10.2991/rare-16.2016.46.

Smart, K.J., Ferrill, D.A., Morris, A.P., 2009, Impact of interlayer slip on fracture prediction from geomechanical models of fault-related folds, American Association of Petroleum Geologists Bulletin, v. 93, p. 1447-1458, https://doi-org.dist.lib.usu.edu/10.1306/05110909034.

Smart, K.J., Ferrill, D.A., Morris, A.P., Bichon, B.J., Riha, D.S., and Huyse, L., 2010, Geomechanical modeling of an extensional fault-propagation fold: Big Brushy Canyon monocline, Sierra Del Carmen, Texas: American Association of Petroleum Geologists Bulletin, v. 94, p. 221–240, DOI: 10.1306/08050908169.

Smart, K.J., Ferrill, D.A., Morris, A.P., and McGinnis, R.N., 2012, Geomechanical modeling of stress and strain evolution during contractional fault-related folding: Tectonophysics, v. 576–577, p. 171–196, DOI: 10.1016/j.tecto.2012.05.024.

Smart, K.J., Ofoegbu, G.I., Morris, A.P., McGinnis, R.N., and Ferrill, D.A., 2014, Geomechanical modeling of hydraulic fracturing: Why mechanical stratigraphy, stress state, and pre-existing structure matter: American Association of Petroleum Geologists Bulletin, v. 98, p. 2237–2261, DOI: 10.1306/07071413118.

Souque, C., Davies R.K., Knipe, R. J.,Welch, M., Lickorish, H., 2008, Detailed Thrust Fault Architecture: Cedar Mountain Thrust, N San Rafael Swell, Utah: American Association of Petroleum Geologists Search and Discovery Article #90078.

Strayer, L.M., Hudleston, P.J., 1997. Numerical modeling of fold initiation at thrust ramps: Journal of Structural Geology, v. 19, p. 551–566.

Suppe, J., 1983, Geometry and kinematics of fault-bend folding: American Journal of Science, v. 283, p. 684–721, DOI: 10.2475/ajs.283.7.684.

Suppe, J., and Medwedeff, D.A., 1990, Geometry and kinematics of fault-propagation folding: Eclogae Geologicae Helvetiae, v. 83, p. 409–454, DOI: 10.1016/j.cnsns.2016.07.026.

Tavani, S., Storti, F., and Salvini, F., 2006, Double-edge fault-propagation folding: geometry and kinematics: Journal of Structural Geology, v. 28, p. 19–35, DOI: 10.1016/j.jsg.2005.09.007.

Teal, R.R., 1983, The triangle zone at Cabin Creek, Alberta Canada: American Association of Petroleum Geologists Studies in Geology, v. 15, DOI: doi.org/10.1306/St15433431432.

Teixell, A., and Koyi, H.A., 2003, Experimental and field study of the effects of lithological contrasts on thrust-related deformation: Tectonics, v. 22, DOI: 10.1029/2002TC001407.

Underwood, C.A., Cooke, M.L., Simo, J.A., and Muldoon, M.A., 2003, Stratigraphic controls on vertical fracture patterns in Silurian dolomite, northeastern Wisconsin: American Association of Petroleum Geologists Bulletin, v. 87, p. 121–142, DOI: 10.1306/072902870121.

Uzkeda, H., Poblet, J., and Bulnes, M., 2010, A geometric and kinematic model for double-edge propagating thrusts involving hanging wall and footwall folding. An example from the Jaca-Pamplona Basin (Southern Pyrenees): Geological Journal, v. 45, p. 506–520, DOI: 10.1002/gj.1205.

Wacker, M.A., 2001, Geometry and kinematics of thrust related drag folds: an example from the San Rafael Swell, Central Utah, Thesis: Florida International University.

Welch, M.J., Knipe, R.J., Souque, C., and Davies, R. K., 2009, A Quadshear kinematic model for folding and clay smear development in fault zones, Tectonophysics, v. 471, p. 186-202. DOI:10.1016/j.tecto.2009.02.008

Wigginton, S.S., 2018, The Influence of Mechanical Stratigraphy on Thrust-Ramp Nucleation and Propagation of Thrust Faults: Master's thesis, Utah State University, Logan, Graduate Theses and Dissertations. 7344, https://digitalcommons.usu.edu/etd/7344.

Williams, G., and Chapman, T., 1983, Strains developed in the hanging walls of thrusts due to their slip/propagation rate: a dislocation model: Journal of Structural Geology, v. 5, p. 563–571, DOI: doi.org/10.1016/0191-8141(83)90068-8.

Witkind, I. J., 1988, Geologic map of the Huntington 30' x 60' quadrangle, Carbon, Emery, Grand and Uintah Counties, Utah, U. S. Geological Survey Map I-1764, scale 1:100,000, https://doi.org/10.3133/i1764.

Woodward, N.B., 1986, Thrust fault geometry of the Snake River Range, Idaho and Wyoming: Geological Society of America Bulletin, v. 97, p. 178-193, DOI:10.1130/0016-7606(1986)97<178:TFGOTS>2.0.CO;2.

Woodward, N.B., and Rutherford, E., 1989, Structural lithic units in external orogenic zones: Tectonophysics, v. 158, p. 247–267, DOI: 10.1016/0040-1951(89)90327-2.

Zhuang, X., Chun, J., and Zhu, H., 2015, A comparative study on unfilled and filled crack propagation for rock-like brittle material, DOI: 10.1016/j.tafmec.2014.04.004.

FIGURE CAPTIONS

Figure 1. Models and interpretations of thrust fault development in anisotropic rocks. A) The early ramp model of Eisenstadt and DePaor (1987) in which thrust faults initiate in the stronger horizons and subsequent shortening is accommodated by linkage in the weakened layers of the early ramps. B) Interpretation of a field expression of upper and lower fault tip to fold transitions from McConnell et al. (1997). C) Fault-tip folding, and lower fault syncline development, from Ferrill et al. (2016).

Figure 2. A geologic map of the Ketobe Knob outcrop area (modified from Wacker, 2001; Witkind, 1998; Petrie et al., 2018). The Ketobe thrust structure is part of a lateral ramp structure that is part of a north-northeast trending thrust complex that cuts gently north, northeast and northwest dipping Jurassic strata at the northern end of the San Rafael Swell, central Utah.

Figure 3. Outcrop view looking to the northwest at the Ketobe Knob thrust. Rocks in the hanging wall display a small anticline above the fault at the northeast side. The footwall is characterized by a small syncline (exposed in dip and strike views). The fault consists of several sub-parallel southward-dipping strands. The fault is exposed in the dip-section on the southeast and northwest sides of the precipice, and the lower tip region is exposed in the strike section along the lower left of this view.

Figure 4. Stratigraphy of the Ketobe Knob outcrop. A) The Entrada and Curtis formations are separated into 5 units based on their sedimentology and mineralogy. B) Schmidt rebound values from each of the 5 units show distinct mechanical strengths, from Wigginton, 2018).

Figure 5. Major reconstruction steps of the 2D cross section restoration in *Move*$^{\text{TM}}$. A) The present day configuration of the outcrop. B-E) Progressive, sequential restoration steps are shown for the preferred model. The preferred model restores with the best line length balance, and fewest gaps that develop during modeling.

Figure 6. Displacement vs distance graphs for the major faults based on the preferred restored cross section. A) the uppermost fault, B) the middle fault and, C) the lowest fault. Shaded area under the curves show the unit cut by the fault. See Figure 4 for color key for units.

Figure 7. Boundary and loading conditions for mechanical models in ABAQUS$^{\text{TM}}$. A) Boundary conditions and loads applied to the stratigraphic package for the unfaulted and faulted models deformed

by pressure loads. The model is ~30 m high and 50 m wide. The model was run with uniform 1 m mesh. B) Boundary conditions applied to the faulted model deformed with a displacement boundary condition. Additional material was added to the base and sides to reduce edge effects. The model was run with 1 m mesh in the interior 50 m and larger mesh in the areas with buffer material.

Figure 8. Model results from unfaulted finite element models with variation in mechanical stratigraphy after the end of the loading step. Interlayer friction coefficient is $\mu = 0.85$. A) Color contours show the maximum compressive stress values. B) Black vectors show the orientation of the maximum principal stress trajectories through the model. C) Plot of stress with depth at the centerline of the model (see Figure 7 for color key).

Figure 9. A) Stress-time and B) stress-strain curves for the intact models. The inflection points on the curves indicate a transition from elastic to plastic deformation. C) Stress as a function of time during the loading step in the units above the upper fault tip (Curtis conglomerate) and below the lower fault tip (Earthy Entrada silty sandstone) in the faulted model shown in Figure 12. D) Graph of stress over time in each unit from Figure 14. Stresses rise rapidly as the load is applied, then levels off for the rest of the loading steps.

Figure 10. Models of unfaulted rocks with variation in mechanical stratigraphy and variations in interlayer friction. A) frictionless slip, B) $\mu = 0.2$, C) $\mu = 0.4$, and D) $\mu = 0.85$. The color contours show the maximum compressive stress. E) Displacement profiles for the left edge of the model at the end of each model run for the different values of μ , as shown.

Figure 11. Stress as a function of time for models of unfaulted rocks with variation in mechanical stratigraphy and variations in interlayer friction. A) frictionless slip, B) $\mu = 0.2$, C) $\mu = 0.4$, and D) $\mu = 0.85$.

Figure 12. Results from faulted FEM with no variation in mechanical stratigraphy after the end of the loading step. Interlayer friction coefficient is $\mu = 0.85$. A) Color contours show the maximum compressive stress. B) Black vectors show the orientation of the maximum principal stress.

Figure 13. Results from the FEM of the faulted model with variation in mechanical stratigraphy. Graph showing stress as a function of time during the loading step for in the units above the upper fault tip (Curtis conglomerate) and below the lower fault tip (Earthy Entrada silty sandstone).

Figure 14. Results from the FEM of the faulted model with variation in mechanical stratigraphy. Interlayer friction is $\mu = 0.85$. In the faulted model we assigned a friction coefficient of $\mu = 0.4$ to the fault surface. A) Color contours show the maximum compressive stress. Areas shaded in black have stresses >300 MPa. B) Black vectors show the orientation of the maximum principal stresses. Stresses are highest in the direct footwall of the lower tip of the fault.

Figure 15. Finite element model with a fault and variations in mechanical strength deformed by a displacement boundary condition. A) Schematic view of the model domain. B) Results of the model showing maximum principal stress in MPa. C) Vectors show the orientation of the maximum principal stress. D) Hanging wall anticline and footwall syncline development at fault tips.

Figure 16. Graph of stress over time in each unit in the finite element model with a fault and variations in mechanical strength deformed by a displacement boundary condition.

Figure 17. Mechanics of stress distribution and potential failure in Mohr-Coulomb space. A) Stress-depth profile for the intact rock model (from Figure 8c). Yellow line indicates the starting applied stress of 200 MPa. B) Representation of stresses in the mechanically stratified section. At the start of the loading $\sigma_1 =$ 200 MPa, and the vertical load, $\sigma_2 = 40$ MPa. As the stresses are applied through the layers, stresses in the weaker horizons (b) drop and increase in the stronger section (c). Failure may occur in the strong section before the weaker rocks in cases where the combination of cohesive and frictional strengths are reached by the increased stresses in the strong section while the weaker rocks experience stress reductions below failure.

Table 1. Schmidt hammer results, and calculated UCS and Young's moduli for the rocks in the study.

Mechanical Unit	**Average Rebound (R)**	**UCS (MPa)**	**E (GPa)**
Curtis SS	38.1	28.4	9.8
Curtis conglomerate	40.7	33.7	12.0
Entrada SS (upper)	49.8	62.1	22.5
Earthy Entrada	39.3	30.7	10.8
Entrada SS (lower)	45.9	47.8	17.5
Conversion Equations[†]		ln(UCS)= 0.792+0.067 x R	ln(E)= -8.967+3.091 x lnR

(UCS) Uniaxial Compressive Stress, (E) Young' Modulus

[†](Aydin and Basu, 2005; Katz et al., 2000)

Table 2. Parameters used for material properties of the rock units

Unit	**UCS (MPa)**[*]	**E (GPa)**[*]	**μ**[*]	***v***[†]	**φ**[†]	**ψ**[†]	**C (MPa)**[§]
Curtis SS.	28.4	9.8	.85	0.2	15	3.7	10.9
Curtis conglomerate	33.7	12.0	.85	0.2	20	5	11.8
Entrada SS. (upper)	62.1	22.5	.85	0.2	25	6.3	19.8
Earthy Entrada Silty SS.	30.7	10.8	.85	0.3	15	3.7	11.8
Entrada SS. (lower)	47.8	17.5	.85	0.2	20	5	16.7

[*] derived from field data

[†] derived from literature

[§] derived from field data and literature

Uniaxial Compressive Stress (UCS), Young's Modulus (E), Static and Kinetic coefficients of friction (μ), Poisson's Ratio (*v*) (Gercek, 2007), Friction Angle (φ) (Smart et al., 2014), and Dilation Angle (ψ) (Smart et al., 2014), Cohesion yield stress (C) (Goodman, 1980) (C=UCS/(2*tan(45+.5* φ)).

Table 3. Pressure loads applied to unfaulted and faulted models

Step	Time Period (s)	σ_1 (MPa)*	σ_3 (MPa) †	Gravity (m/s^2)
1 (Gravity)	0-1	-	-	-9.80
2 (Pressure)	1-2	200	40	-9.80

*σ_1 is horizontal
†σ_3 is vertical (downward)
Fault µ = 0.85

Table 4. Loads applied to the faulted model deformed with a displacement load

Step	Time (s)	σ1 (MPa)*	σ3 (MPa)†	Gravity (m/s2)	Displacement (m)
Initial	0	52	40	-	-
1 (Gravity)	0-1	52	40	-9.80	-
2 (Displacement)	1-2	52	40	-9.80	2

*σ_1 is horizontal
†σ_3 is vertical (downward)
Fault µ = 0.85

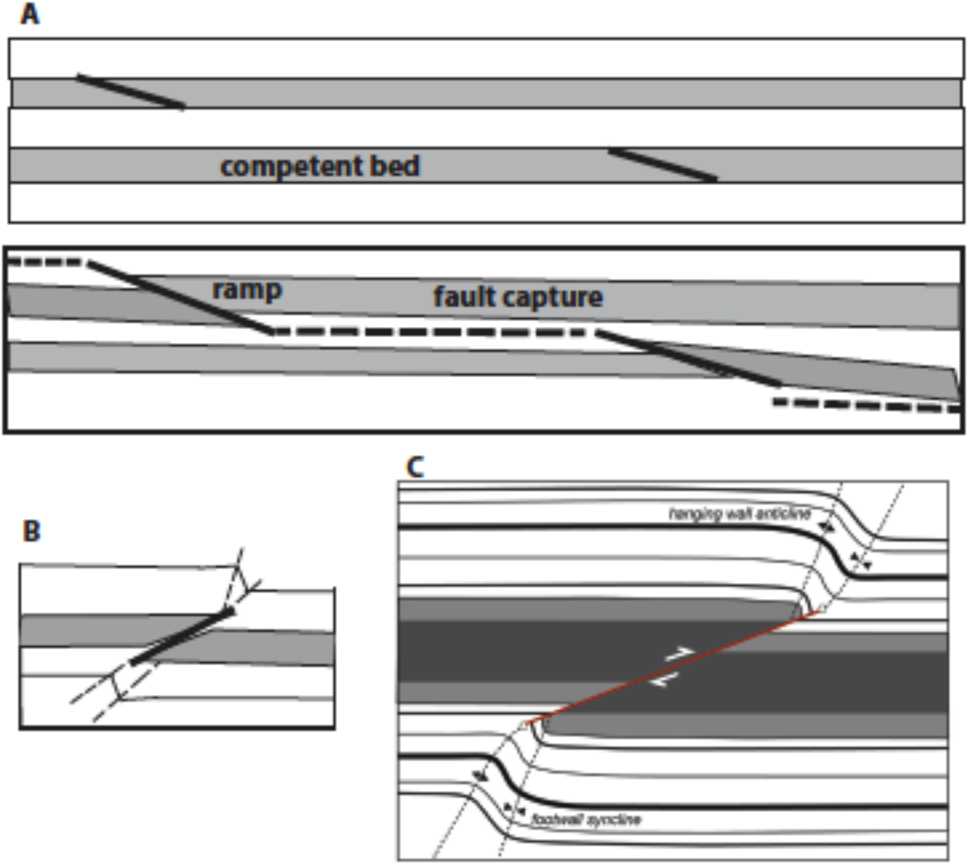
A
competent bed
ramp
fault capture
B
C
hanging wall anticline
footwall syncline

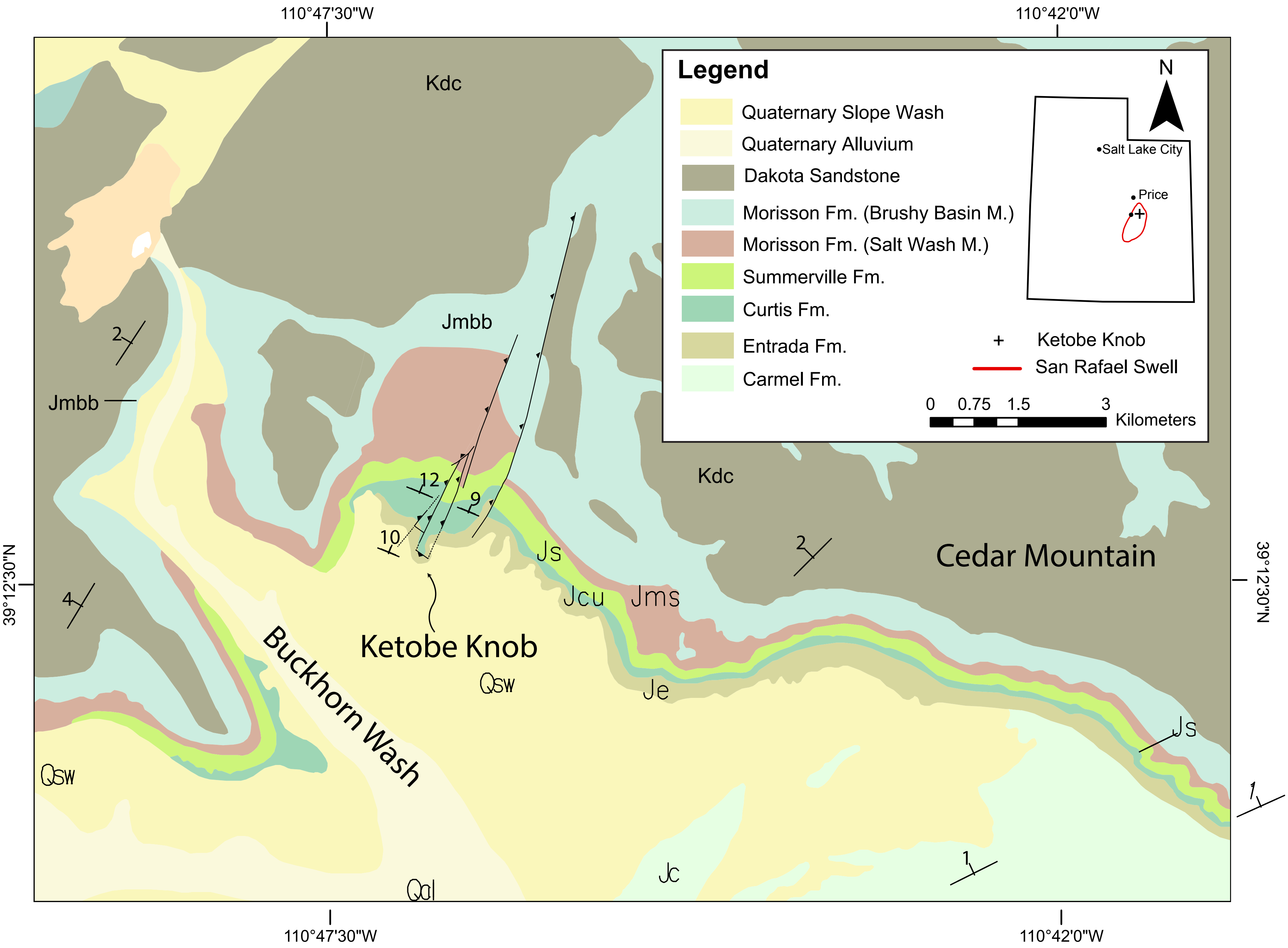
110°47'30"W
110°42'0"W
39°12'30"N
39°12'30"N
110°47'30"W
110°42'0"W
Legend
Quaternary Slope Wash
Quaternary Alluvium
Dakota Sandstone
Morisson Fm. (Brushy Basin M.)
Morisson Fm. (Salt Wash M.)
Summerville Fm.
Curtis Fm.
Entrada Fm.
Carmel Fm.
N
Salt Lake City
Price
+ Ketobe Knob
San Rafael Swell
0
0.75
1.5
3
Kilometers
Kdc
Jmbb
Jmbb
Kdc
2
4
12
9
10
2
Js
Jcu
Jms
Cedar Mountain
Ketobe Knob
Buckhorn Wash
Qsw
Je
Qsw
Js
1
1
Jc
Qal

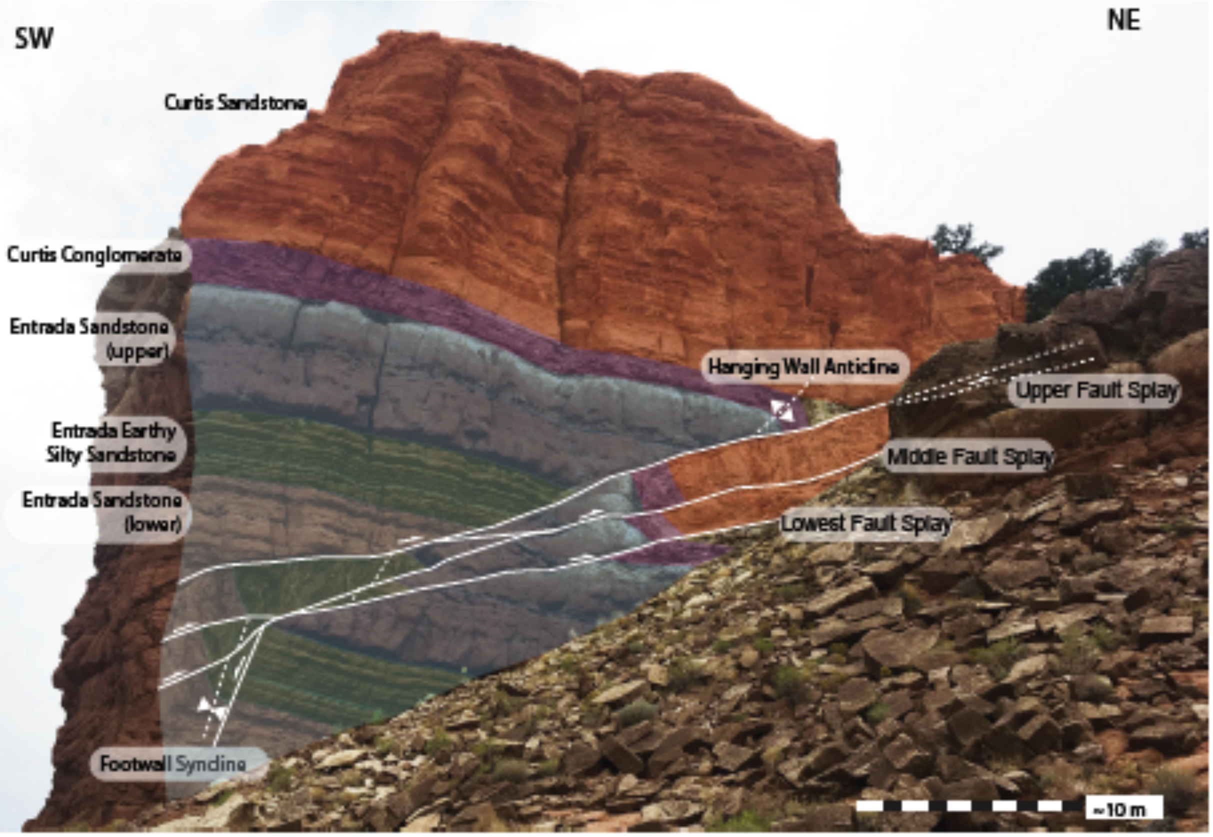
SW
NE
Curtis Sandstone
Curtis Conglomerate
Entrada Sandstone (upper)
Hanging Wall Anticline
Upper Fault Splay
Entrada Earthy Silty Sandstone
Middle Fault Splay
Entrada Sandstone (lower)
Lowest Fault Splay
Footwall Syncline
~10 m

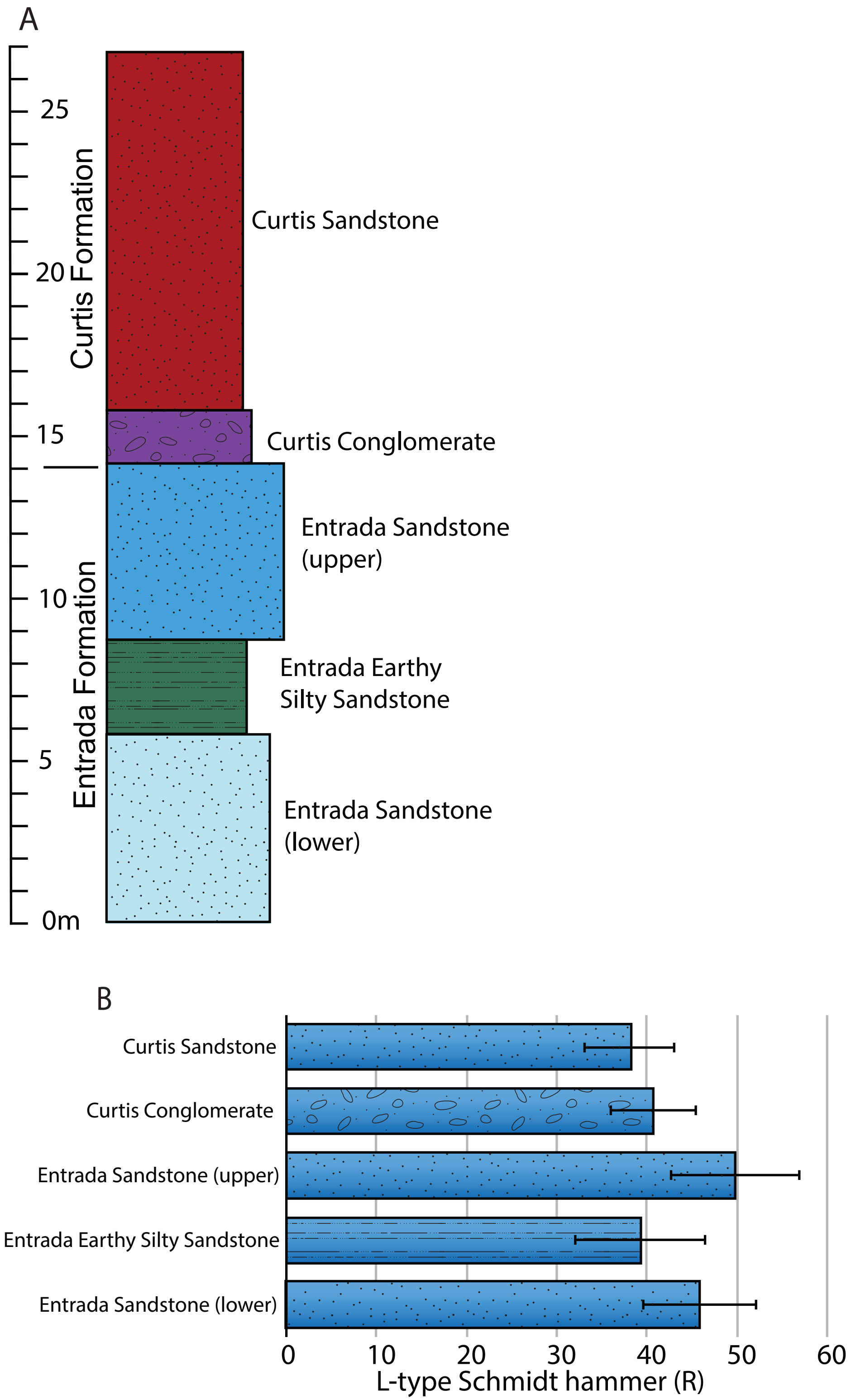

Figure 4. Wigginton et al., 2021 preprint 22 July 2021

A. Final state section. The middle fault formed between the upper and lower faults. The entire region was uplifted, and bedding was tilted (~10 ° bed dip) from the uplift of the San Rafael Swell. This is the outcrop as it appears today in its deformed state.

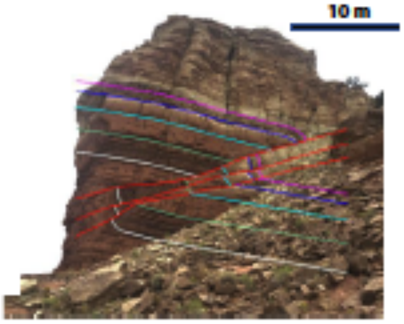

B. Progressive displacement on the lower fault, layers in-between the upper and lower fault were steeply tilted.

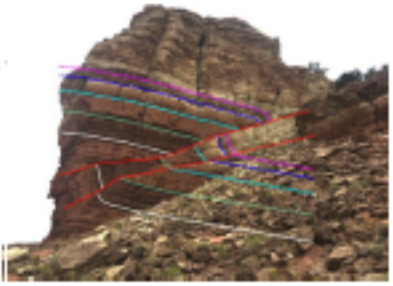

C. Nucleation on the lower fault near the base of the upper Entrada sandstone propagated upward and downward. The downward propagation of the fault created a footwall syncline in the Earthy Entrada silty sandstone.

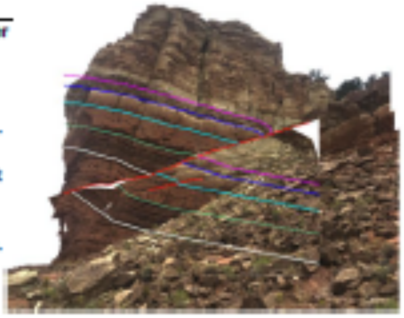

D. The upper fault nucleated first in the upper Entrada sandstone, then propagated upward and downward. The upward propagation of the fault created a hanging wall anticline in the Curtis conglomerate. The upper fault forming first is consistent with kinematic models of thrust fault imbricates (where the highest stratigraphic fault is the earliest formed).

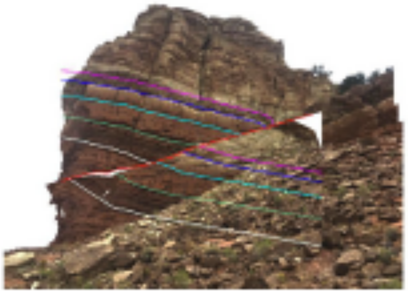

E. Original state section. Some gentle folding of the layers is interpreted to be present prior to faulting, with a very shallow regional north dip preserved.

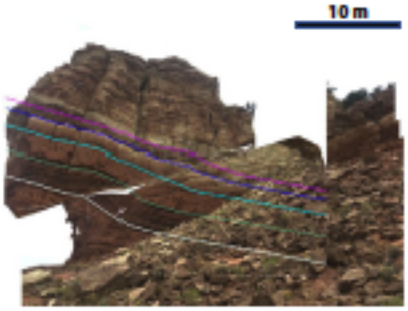

Figure 5. Major reconstruction steps of the 2D cross section restoration in *Move*™. A) The present day configuration of the outcrop. B-E) Progressive, sequential restoration steps are shown for the preferred model. The preferred model restores with the best line length balance, and fewest gaps that develop during modeling.

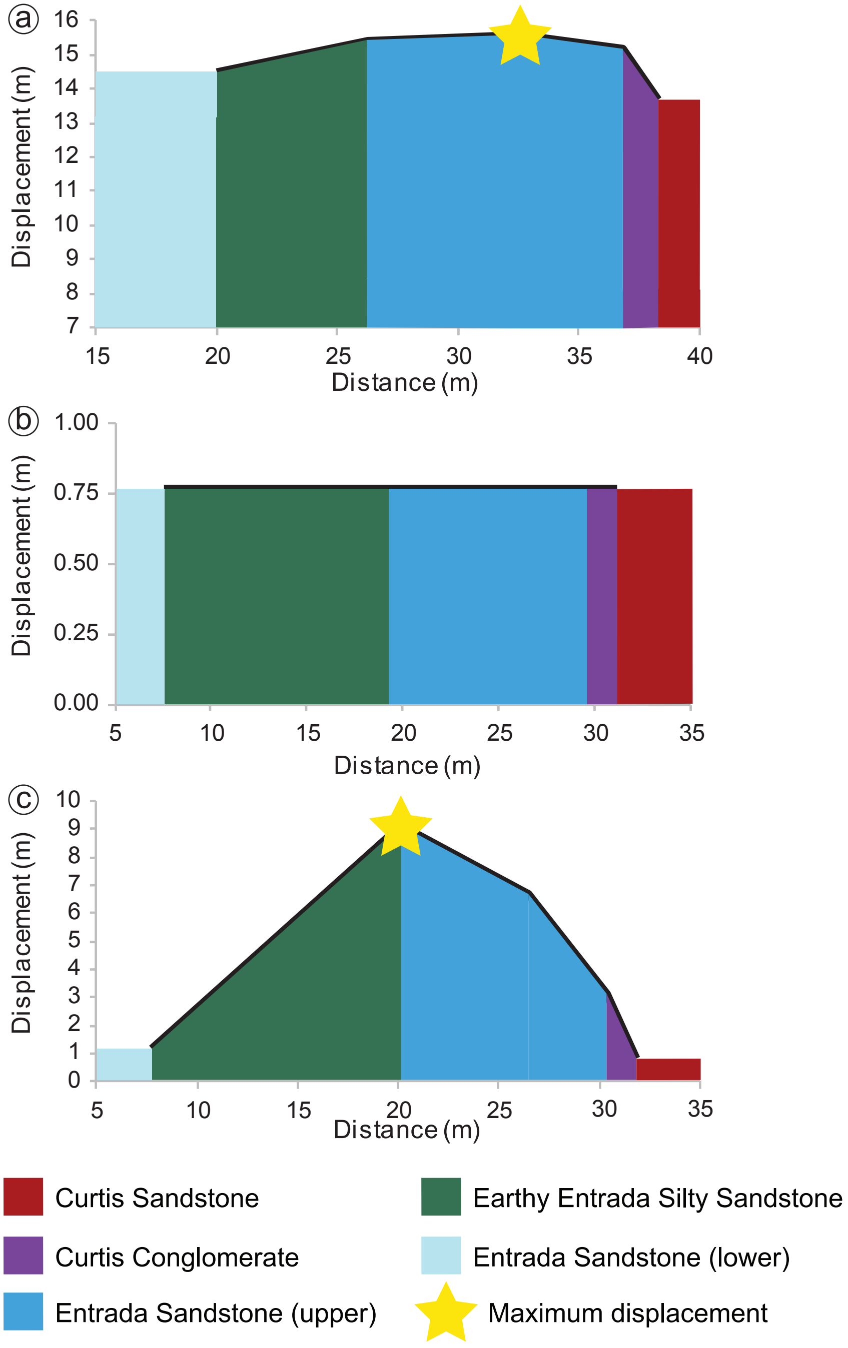
ⓐ
Displacement (m)
16
15
14
13
12
11
10
9
8
7
15
20
25
30
35
40
Distance (m)
ⓑ
Displacement (m)
1.00
0.75
0.50
0.25
0.00
5
10
15
20
25
30
35
Distance (m)
ⓒ
Displacement (m)
10
9
8
7
6
5
4
3
2
1
0
5
10
15
20
25
30
35
Distance (m)
Curtis Sandstone
Curtis Conglomerate
Entrada Sandstone (upper)
Earthy Entrada Silty Sandstone
Entrada Sandstone (lower)
Maximum displacement

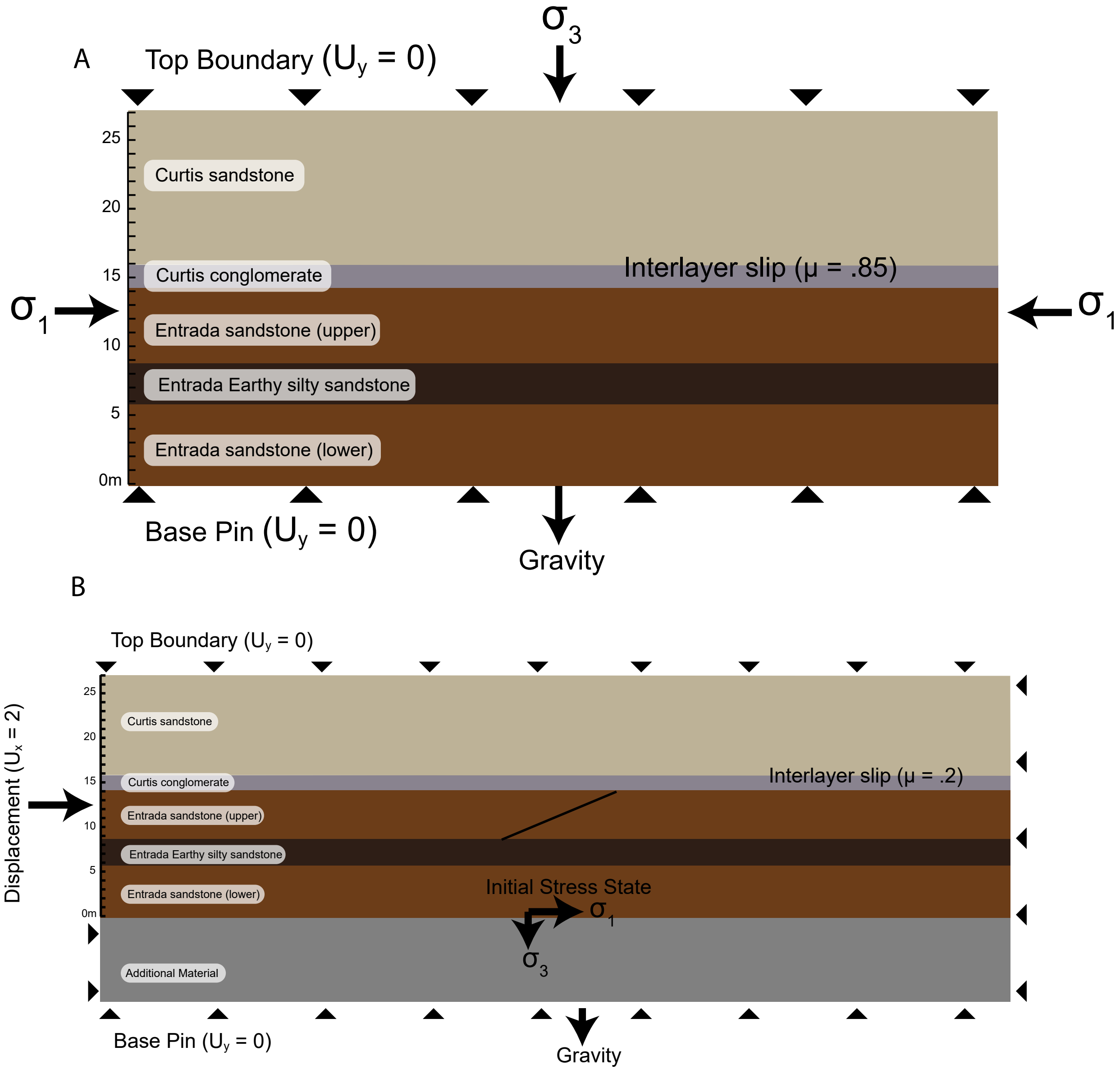

Figure 7. Wigginton et al.,

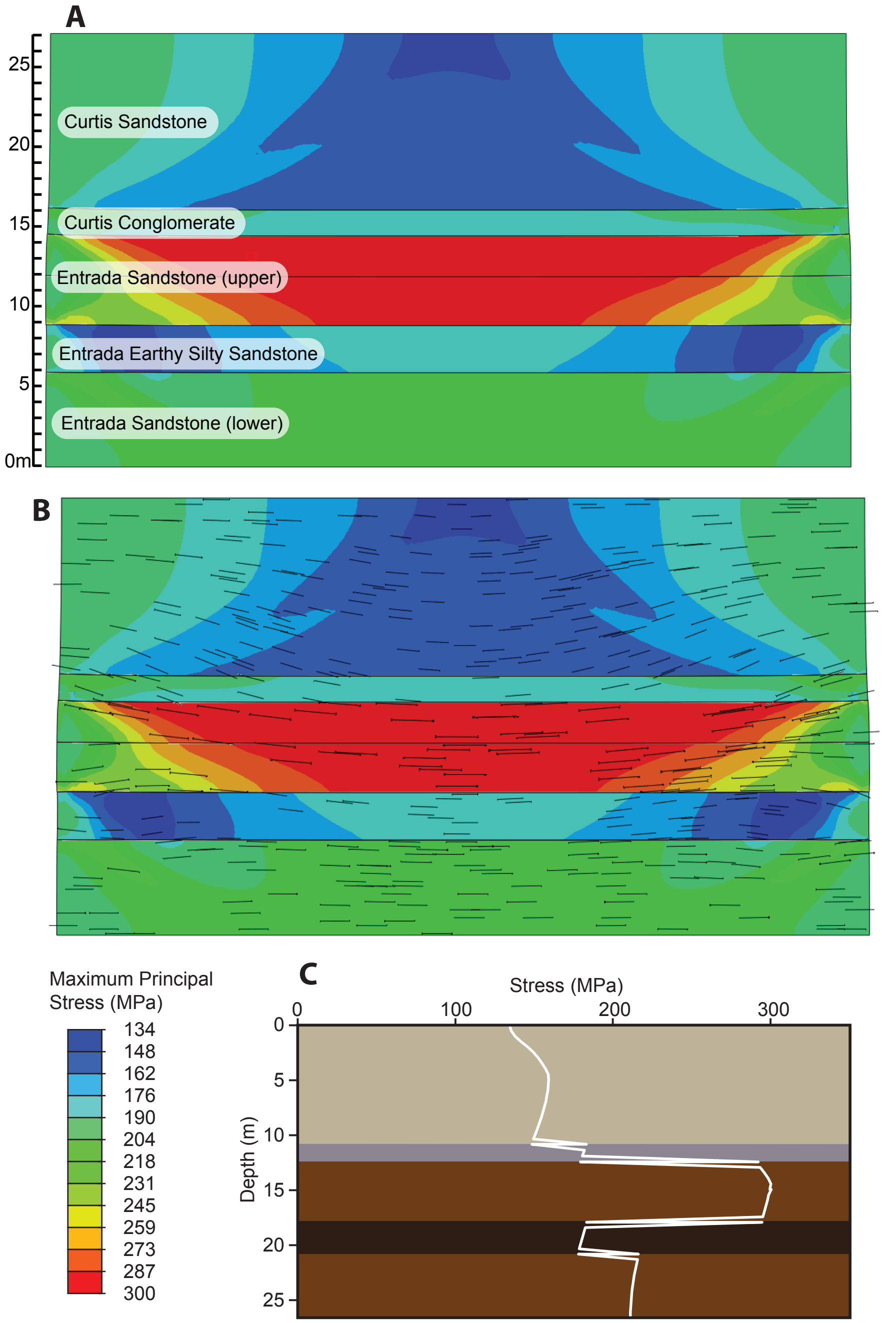
A
25
20
15
10
5
0m
Curtis Sandstone
Curtis Conglomerate
Entrada Sandstone (upper)
Entrada Earthy Silty Sandstone
Entrada Sandstone (lower)
B
Maximum Principal Stress (MPa)
134
148
162
176
190
204
218
231
245
259
273
287
300
C
Stress (MPa)
0
100
200
300
Depth (m)
0
5
10
15
20
25

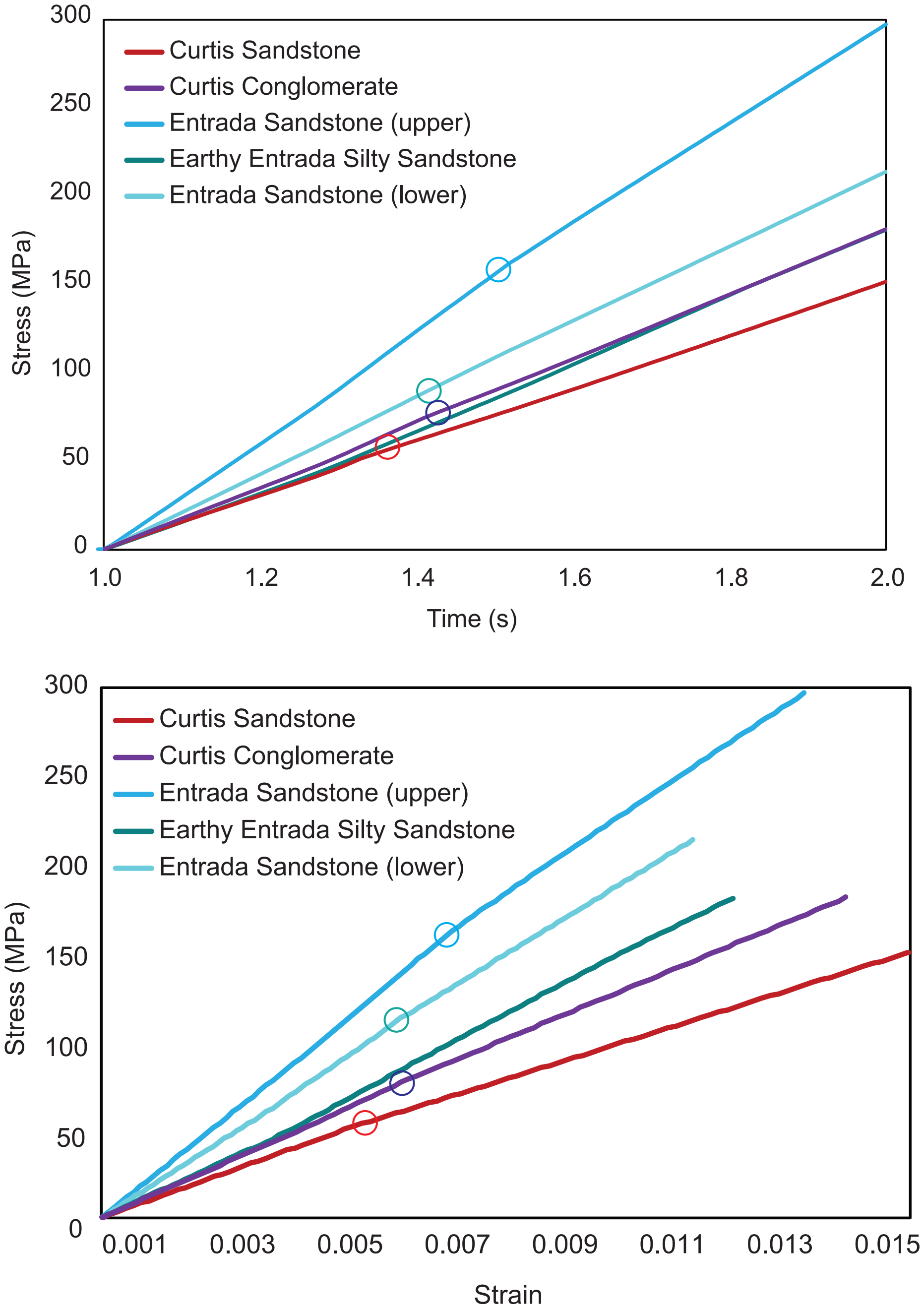

Figure 9. Wigginton et al.,

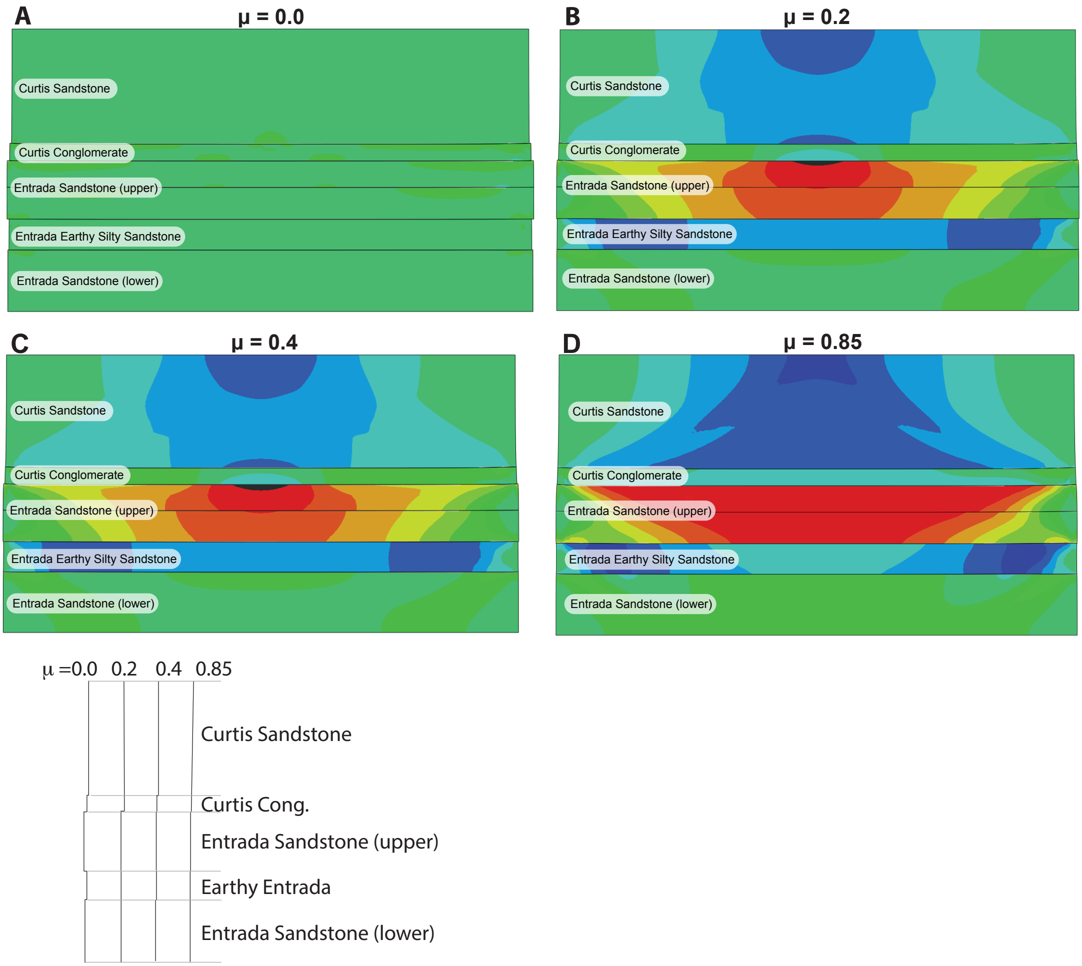
A
μ = 0.0
B
μ = 0.2
C
μ = 0.4
D
μ = 0.85
Curtis Sandstone
Curtis Conglomerate
Entrada Sandstone (upper)
Entrada Earthy Silty Sandstone
Entrada Sandstone (lower)
μ =0.0 0.2 0.4 0.85
Curtis Sandstone
Curtis Cong.
Entrada Sandstone (upper)
Earthy Entrada
Entrada Sandstone (lower)

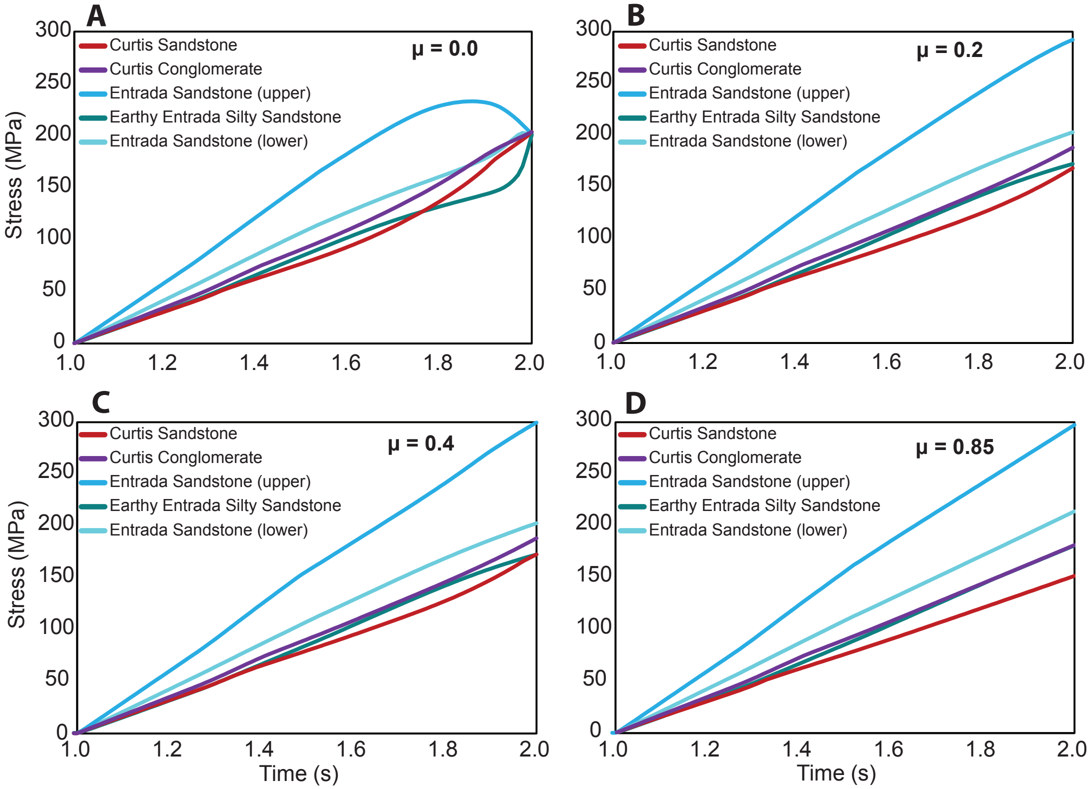
A
μ = 0.0
B
μ = 0.2
C
μ = 0.4
D
μ = 0.85
Curtis Sandstone
Curtis Conglomerate
Entrada Sandstone (upper)
Earthy Entrada Silty Sandstone
Entrada Sandstone (lower)
Stress (MPa)
Time (s)
0
50
100
150
200
250
300
1.0
1.2
1.4
1.6
1.8
2.0

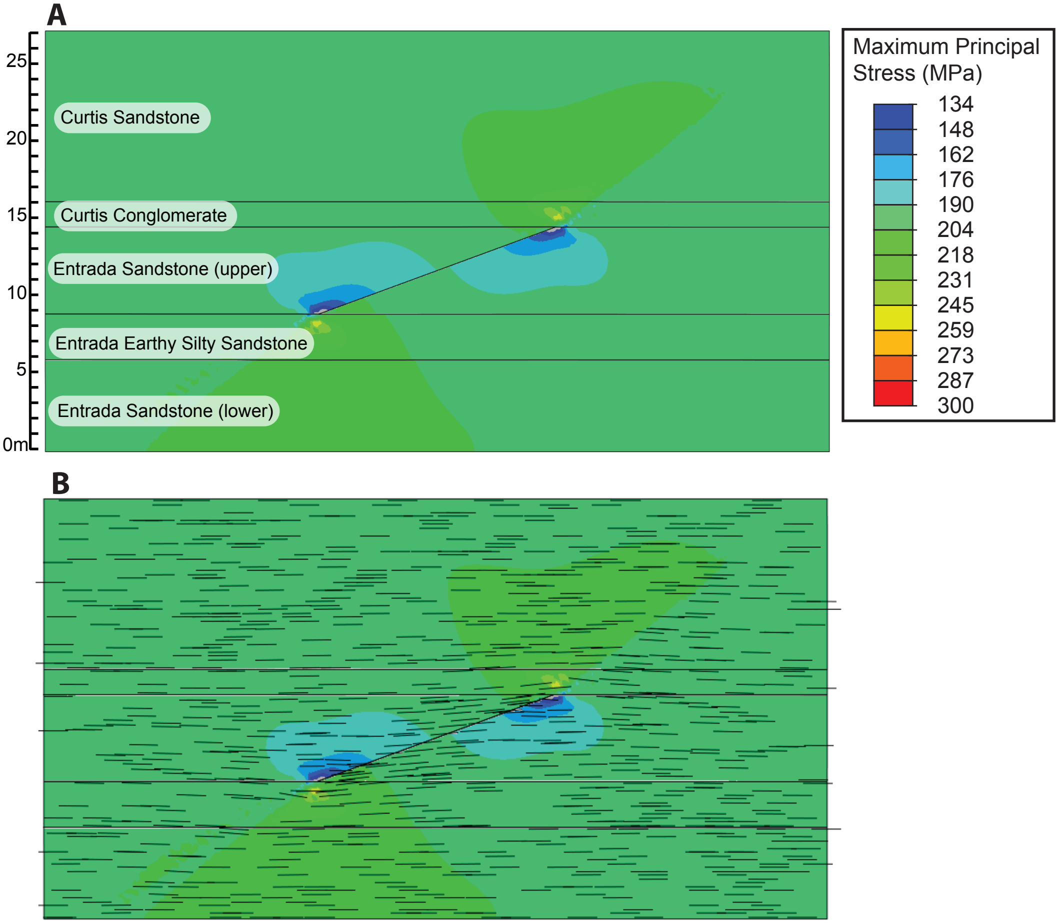
A
25
20
15
10
5
0m
Curtis Sandstone
Curtis Conglomerate
Entrada Sandstone (upper)
Entrada Earthy Silty Sandstone
Entrada Sandstone (lower)
Maximum Principal Stress (MPa)
134
148
162
176
190
204
218
231
245
259
273
287
300
B

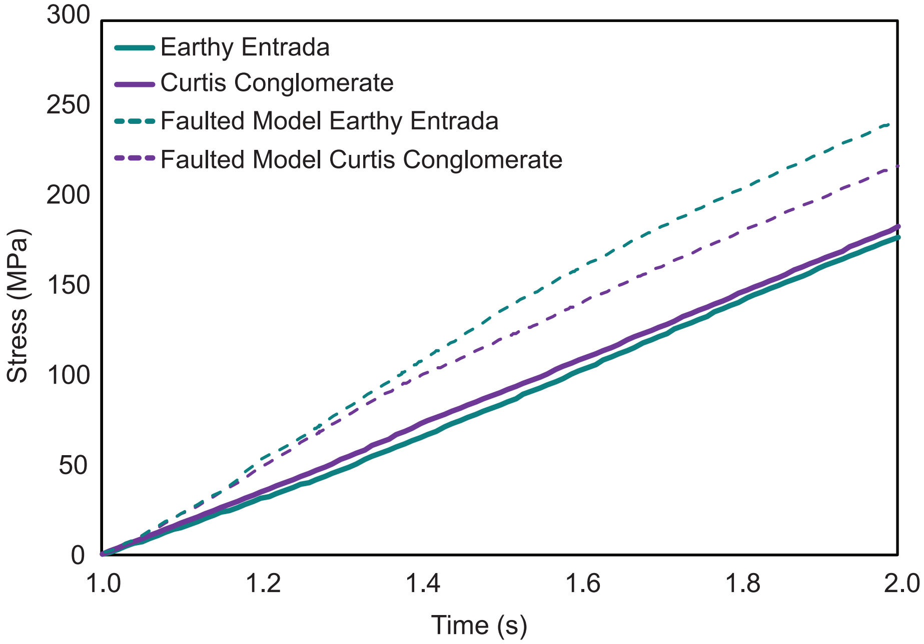
300
250
200
150
100
50
0
Stress (MPa)
1.0
1.2
1.4
1.6
1.8
2.0
Time (s)
Earthy Entrada
Curtis Conglomerate
Faulted Model Earthy Entrada
Faulted Model Curtis Conglomerate

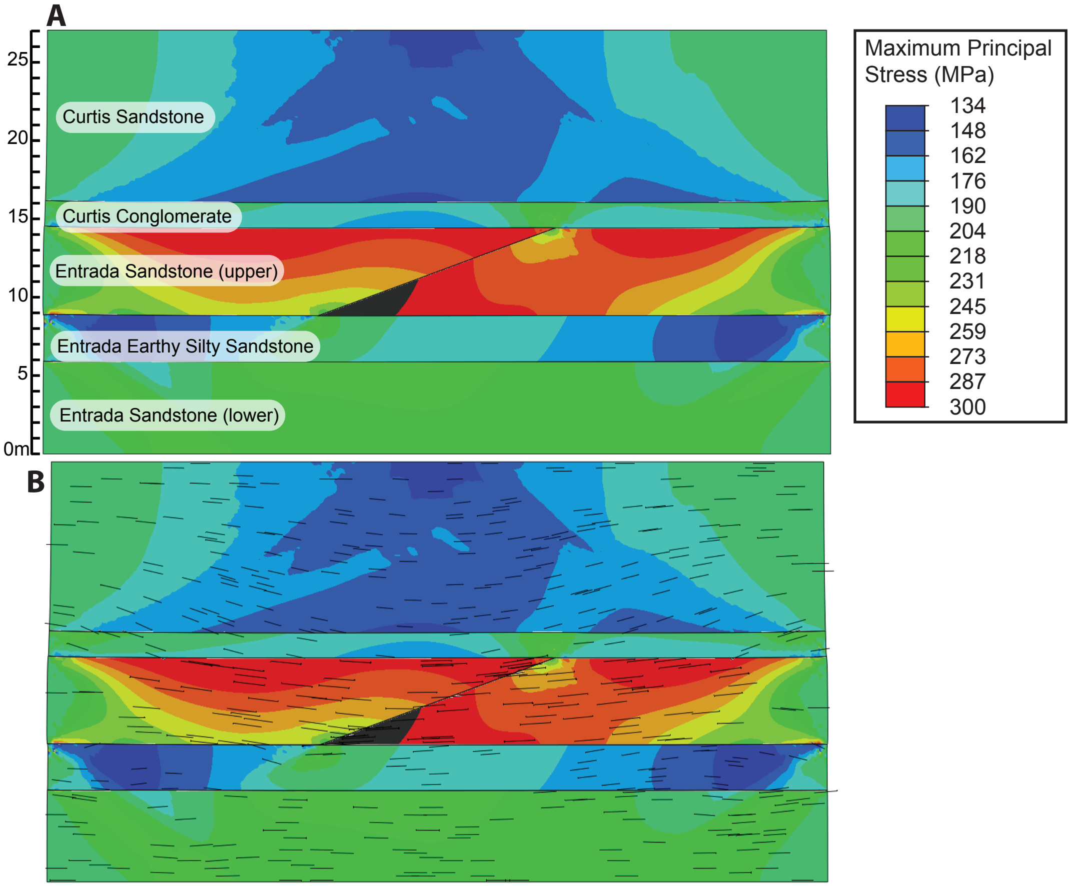
A
25
20
15
10
5
0m
Curtis Sandstone
Curtis Conglomerate
Entrada Sandstone (upper)
Entrada Earthy Silty Sandstone
Entrada Sandstone (lower)
Maximum Principal Stress (MPa)
134
148
162
176
190
204
218
231
245
259
273
287
300
B

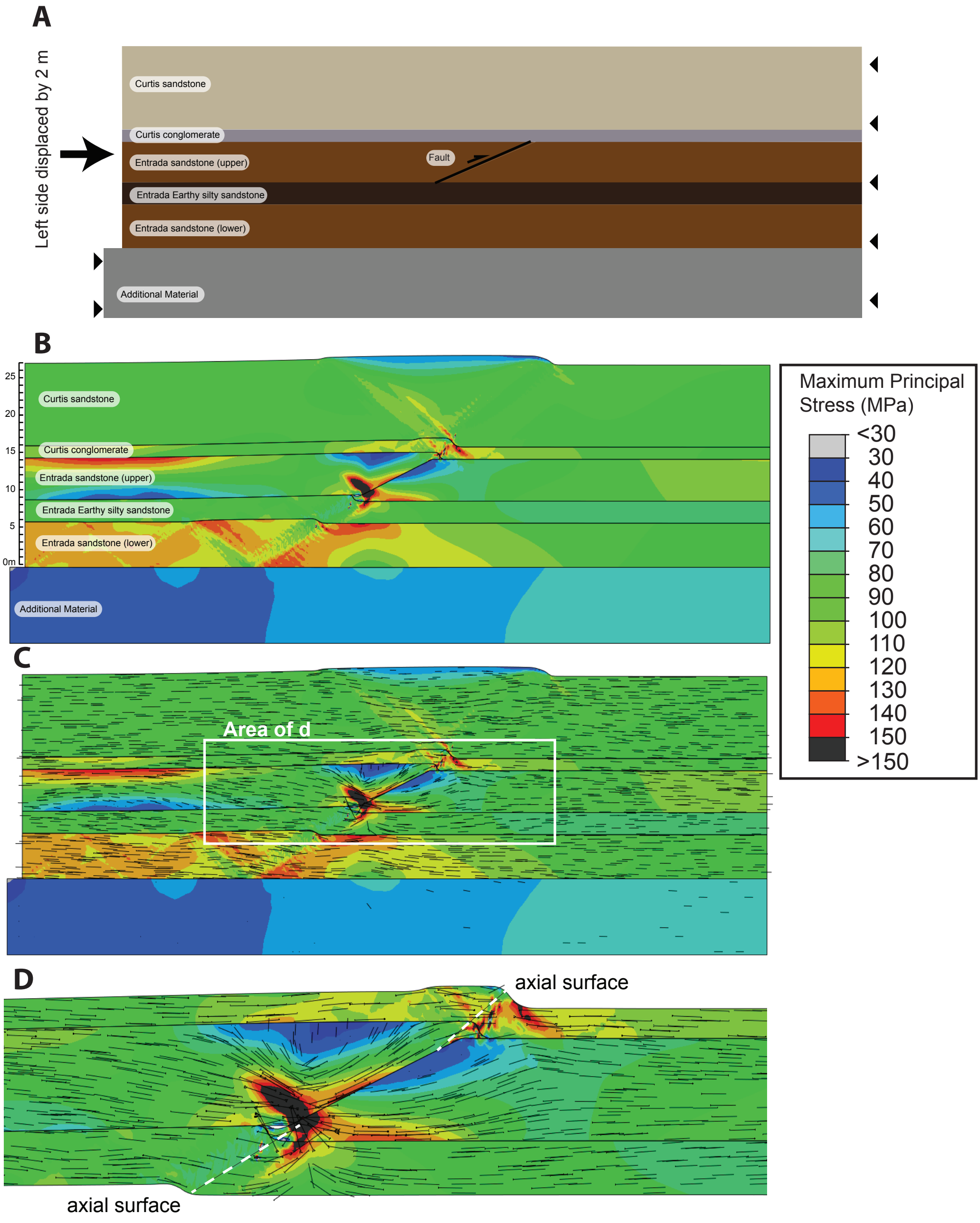
A
Left side displaced by 2 m
Curtis sandstone
Curtis conglomerate
Entrada sandstone (upper)
Fault
Entrada Earthy silty sandstone
Entrada sandstone (lower)
Additional Material
B
25
20
15
10
5
0m
Curtis sandstone
Curtis conglomerate
Entrada sandstone (upper)
Entrada Earthy silty sandstone
Entrada sandstone (lower)
Additional Material
Maximum Principal Stress (MPa)
<30
30
40
50
60
70
80
90
100
110
120
130
140
150
>150
C
Area of d
D
axial surface
axial surface

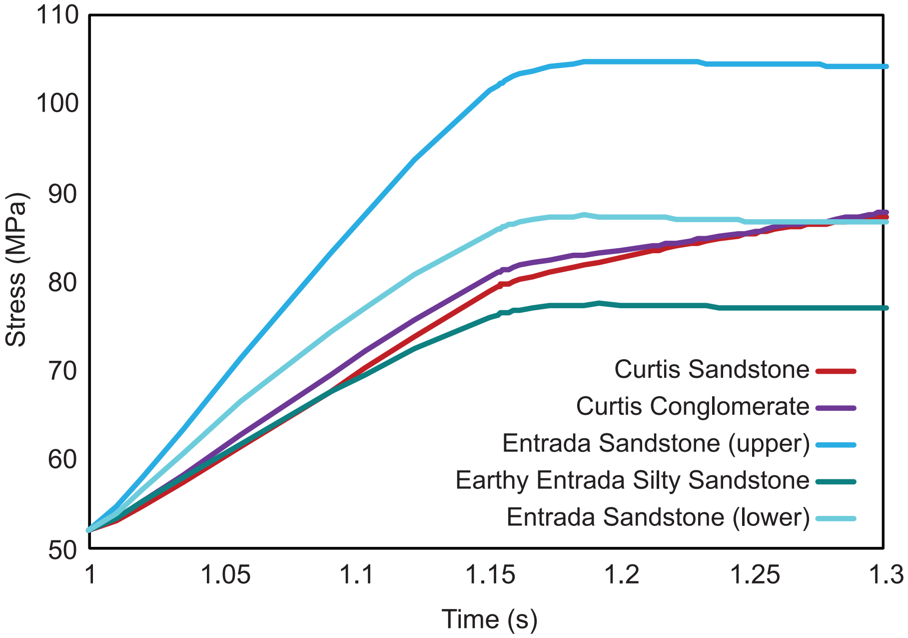

Figure 16. Wigginton et al., 2021 preprint 22 July 2021

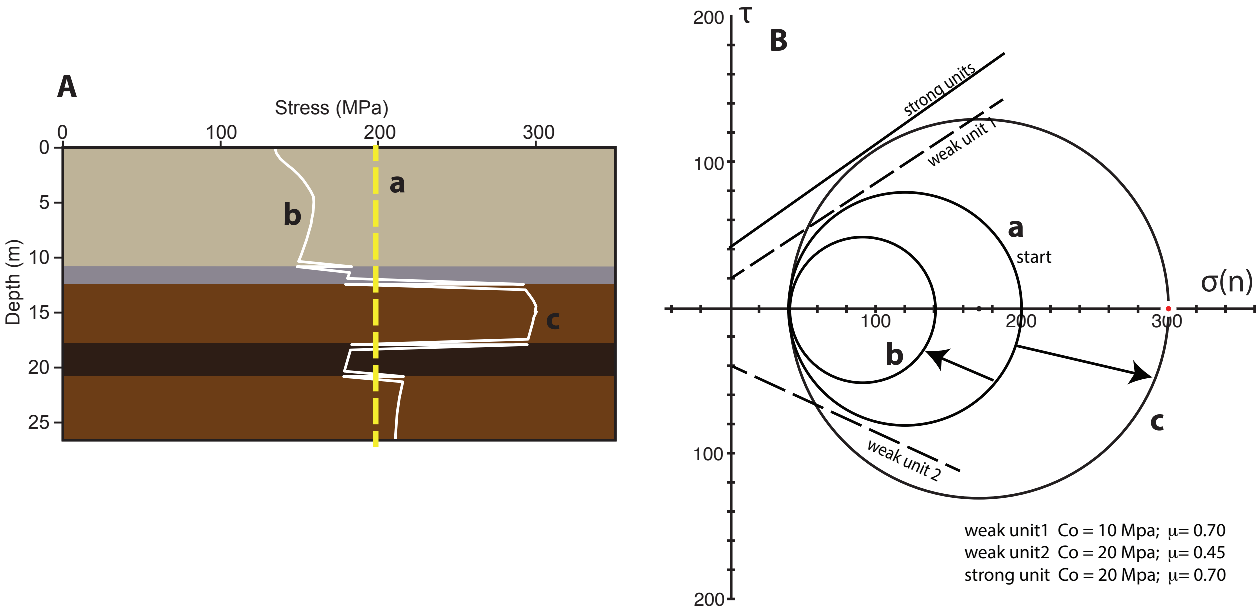

Figure 17. Wigginton et al., 2021 preprint 22 July 2021